Progress In Electromagnetics Research M, Vol. 85, 185–194, 2019

Artificial Dielectric Superstrate Loaded Antenna for Enhanced Radiation Performance

Devassy Tony[1], Valiyaveettil P. Sarin[2], Neeraj K. Pushkaran[1], Kokkadan J. Nelson[1], Pezholil Mohanan[1], and Kesavath Vasudevan[1, *]

Abstract—This paper presents a novel engineered artificial dielectric superstrate for improving the radiation characteristics of a CPW-fed planar antenna. Even though the permittivity of the material used for the superstrate is only 4.4, it attains an effective permittivity of more than 18 because of the periodic pattern printed on it. Due to the high value of effective permittivity, an improvement in radiation pattern, impedance matching, and gain of the antenna are obtained. From the measured results, an impedance bandwidth of 374 MHz from 2.453 GHz to 2.827 GHz is observed for the antenna loaded with superstrate. The periodic pattern is fabricated on a substrate of thickness 1.6 mm, and it occupies an area of $56.45 \times 42.48\,\text{mm}^2$.

1. INTRODUCTION

The performance of printed circuit antennas used for outdoor applications were affected by environmental hazards, severe weather conditions, etc. A superstrate layer, also called a cover layer has been used to protect the antenna from these threats. Initially, it was assumed that when we used a cover layer, it would adversely affect the matching and radiation performance of the antenna. Alexopoulos and Jackson showed that by a proper selection of superstrate layer, it was possible to enhance the radiation parameters of printed antennas [1]. In [2], transmission line analogy was used to explain radiation from superstrate loaded antenna structure. There the authors established two dual resonance conditions for substrate-superstrate printed antenna geometry by which better gain could be achieved for a high value of permittivity or permeability of the superstrate. In [3], the authors performed a comparative study of three superstrates, namely double negative slab, frequency selective surface, and plain dielectric slab for improving directivity of microstrip antennas. The authors came to the conclusion that the physical mechanism behind directivity enhancement was not the focussing effect of superstrate alone. They attributed the directivity enhancement to the resonance resulting from Fabry-Perot resonant cavity formed by the superstrate and metallic ground plane. Researchers started showing greater interest in developing new methods by which antenna parameters can be improved by manipulating material parameters of superstrates as well as by other means [4–13, 16]. They successfully implemented superstrates in beam steering, enhancing gain, and improving bandwidth. Some authors proposed EBG structures as superstrates for improving antenna parameters [4, 5, 17]. But the thickness of the antenna was the main barrier for these structures. Kim et al. proposed a holey dielectric superstrate for enhancing the gain of a microstrip patch antenna [8]. The effective permittivity was controlled by changing the radius of holes in the superstrate so as to generate an in-phase electric field which resulted in improved gain.

In this paper, a technique for improving the radiation parameters of a CPW-fed planar antenna using a non-resonant superstrate is proposed. It is based on a novel engineered artificial dielectric with

Received 28 June 2019, Accepted 24 September 2019, Scheduled 5 October 2019

* Corresponding author: Kesavath Vasudevan (vasudevankdr@gmail.com).

[1] Department of Electronics, Cochin University of Science and Technology, Cochin-22, Kerala, India. [2] Government College, Chittur, Palakkad, Kerala, India.

high value of effective permittivity. When we load an antenna with a superstrate layer having a high value of permittivity or permeability, the gain can be enhanced [1, 2]. Simulated and experimental results are presented. The effect of artificial dielectric on antenna reflection characteristics, gain, and radiation pattern are investigated.

2. PERIODIC PATTERN DESIGN

For the construction of artificial dielectric, a periodic pattern is used. The pattern consists of 3×4 array of unit cells. The geometry of the unit cell is formed in the following manner. Consider two cylinders of same radius 2 mm and another one of radius 6 mm. All the cylinders are of negligible thickness and made up of highly conductive material. They are placed at the centre of an FR-4 substrate of size $14 \times 14 \times 1.6\,\text{mm}^3$ and relative permittivity 4.4. The thickness of the metallization etched on the substrate is 35 µm. The two cylinders of radius 2 mm are shifted by 4.2 mm in opposite directions along a straight line which makes an angle 45° with Y axis (Fig. 1).

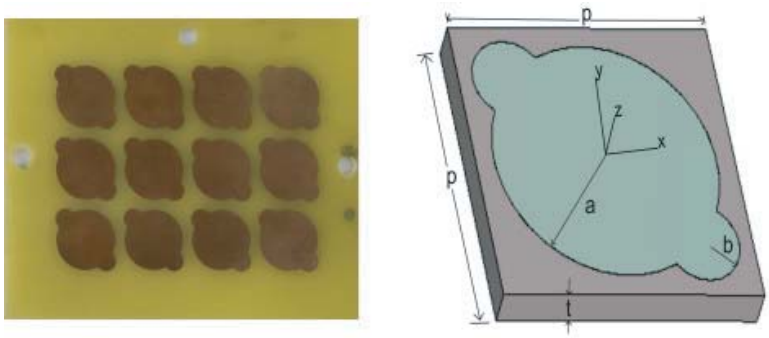

Figure 1. Photograph of the superstrate and unit cell description. $p = 14$, $a = 6$ and $b = 2$ (units in mm).

The array pattern is printed on an FR-4 substrate with relative permittivity 4.4, thickness 1.6 mm, and occupies an area of $56.45 \times 42.48\,\text{mm}^2$. For computing scattering parameters (S parameters) of the periodic pattern by simulation, CST Microwave Studio is used. Along X and Y directions unit cell boundary conditions are applied. These are combined with open boundaries along Z directions. The open boundaries are realized by Floquet mode waveguide ports which can be used for exciting plane waves (Fig. 2).

For characterising artificially engineered materials retrieval of effective permittivity and effective permeability is required. The usual method is to use S parameters calculated from the incident wave

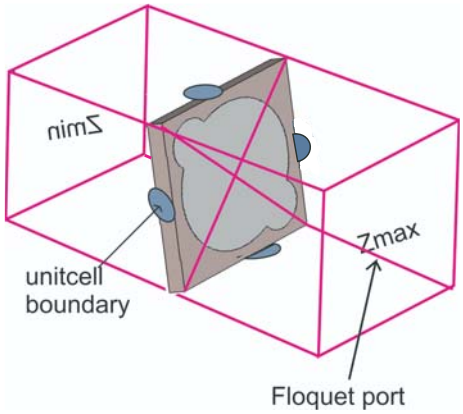

Figure 2. Assignment of Floquet ports and unit cell boundary.

to obtain effective refractive index n and impedance z. The effective permittivity and permeability can then be calculated directly from the expressions $\mu = nz$ and $\epsilon = n/z$.

The refractive index n and impedance z of a slab of material can be obtained from the following expressions [14, 15],

$$z = \pm\sqrt{\frac{(1+S_{11})^2 - S_{21}^2}{(1-S_{11})^2 - S_{21}^2}} \tag{1}$$

$$e^{ink_0d} = X \pm i\sqrt{1-X^2} \tag{2}$$

where $X = 1/2S_{21}(1 - S_{11}^2 + S_{21}^2)$. k_0 denotes the wave number of the incident wave in free space, and d is the thickness of the slab. For a passive medium, the signs of the above equations are determined by the requirement

$$z' \geq 0 \tag{3}$$

$$n'' \geq 0 \tag{4}$$

where $(.)'$ and $(.)''$ denote the real part and imaginary part operators, respectively. Since Equation (2) is a complex exponential, inverting it will result in a multivalued logarithmic function. Solving for refractive index we get

$$n = \frac{1}{k_0 d}\left\{\left[\left[\ln\left(e^{ink_0d}\right)\right]'' + 2m\pi\right] - i\left[\ln\left(e^{ink_0d}\right)\right]'\right\} \tag{5}$$

where m is the branch number of n'.

When we use the above equations for a nonhomogeneous slab, some issues need to be addressed. We have to determine the location of the two boundaries of the effective slab. The retrieval method will fail if the S parameters obtained are noisy. Another issue is ambiguous nature of n' because the logarithmic function is multivalued. All these issues are addressed in [14].

The magnitudes of reflection and transmission characteristics are illustrated in Fig. 3. No resonances are observed in the frequency range shown in figure. Extracted values of effective permittivity and effective permeability are shown in Fig. 4. In [15], the medium is described as having effective permittivity independent of frequency whereas the effective permeability is a function of frequency. From Fig. 4 it is clear that the same pattern can also be observed here, though the magnetic response of the superstrate medium is very feeble. The effective permittivity of the superstrate medium is a function of inter-cell capacitance.

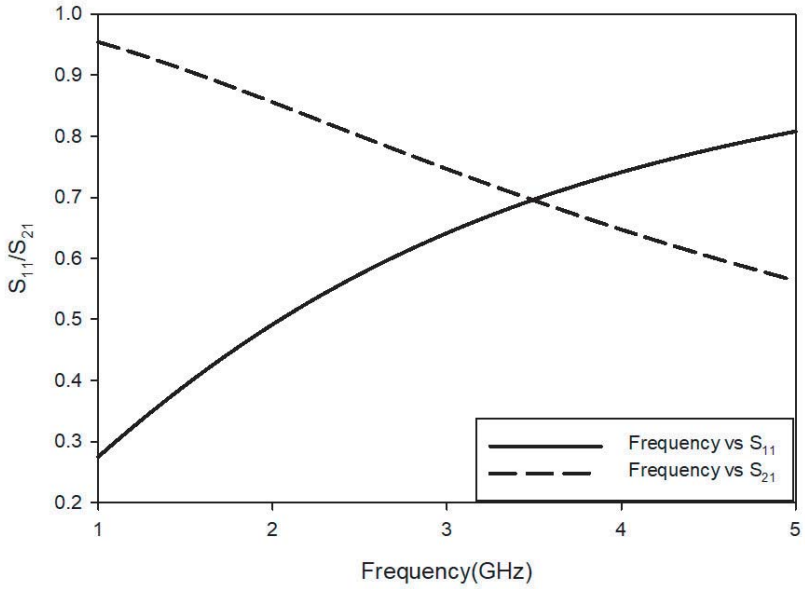

Figure 3. Reflection and transmission characteristics of the unit cell.

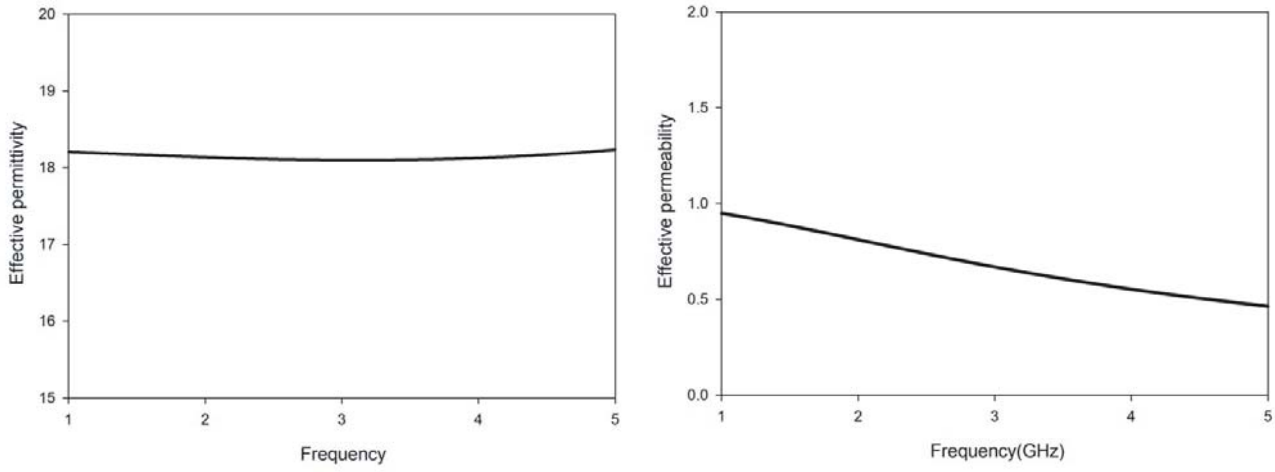

Figure 4. Extracted values of (a) effective permittivity and (b) effective permeability.

3. THE REFERENCE ANTENNA DESIGN

The reference antenna shown in Fig. 5 can be obtained from a standard CPW transmission line by applying a few modifications. First, a 50 Ω CPW transmission line is designed. Standard design equations are used to determine centre conductor width (Wf) and the gap (g) between finite ground planes and centre conductor [18]. The two finite ground planes ($g1$ and $g2$) on either side of the centre conductor are of equal size ($Wg \times Lg$). For a wide range of frequencies extending up to several GHz, there is no resonance observed for this transmission line. The ground $g1$ is connected to the centre conductor using a short of width t to generate a resonance around 3.4 GHz. The resonance can be brought to a lower frequency region by carving out a slot of length Ls in ground $g1$. The reference antenna is printed on an FR-4 substrate with a dielectric constant of 4.4. Overall size of the substrate is $45 \times 21 \times 1.6\,\text{mm}^3$.

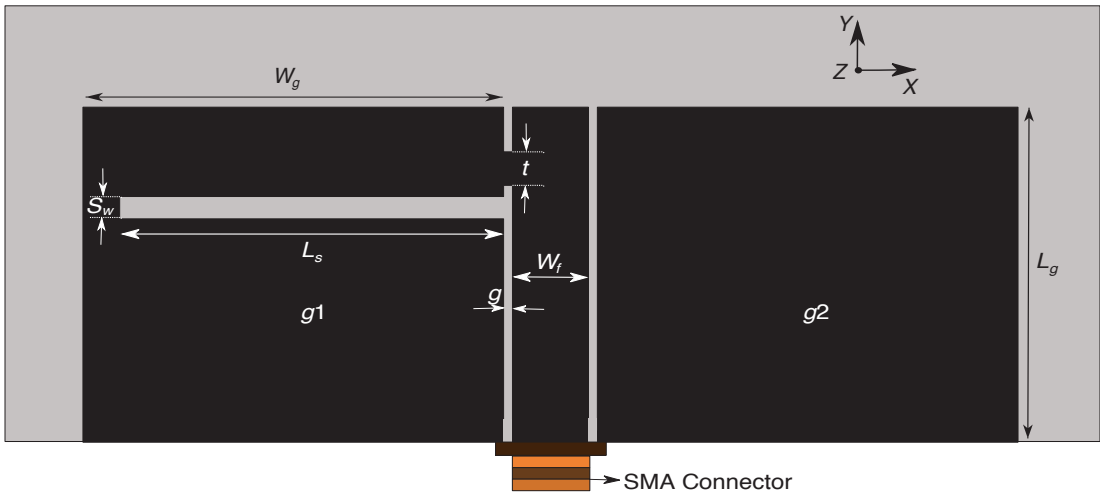

Figure 5. Top view of the reference antenna. $L_s = 13.15$, $L_g = 15$, $S_w = 1$, $W_f = 3$, $W_g = 16.6$, $g = 0.35$ and $t = 1.5$ (units in mm).

4. RESULTS AND DISCUSSIONS

4.1. Reference Antenna

The simulated and measured reflection characteristics of the antenna is shown in Fig. 6. From the measured results, an impedance bandwidth of 325 MHz from 2.5 GHz to 2.825 GHz is observed. The co- and cross-polar radiation patterns of the reference antenna for XZ and YZ planes at 2.62 GHz are shown in Fig. 7. Cross-polar isolation of more than 10 dB along boresight is observed in both planes.

The surface current distribution of the reference antenna at resonance is shown in Fig. 8. The

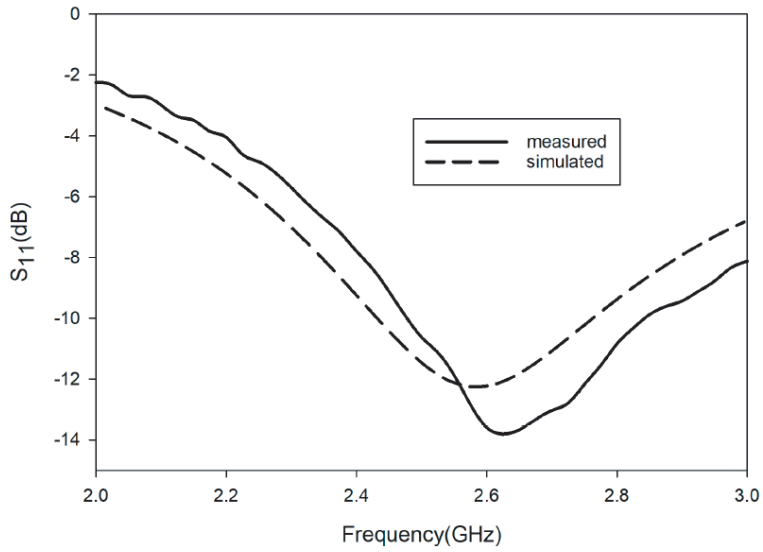

Figure 6. Measured and simulated reflection characteristics.

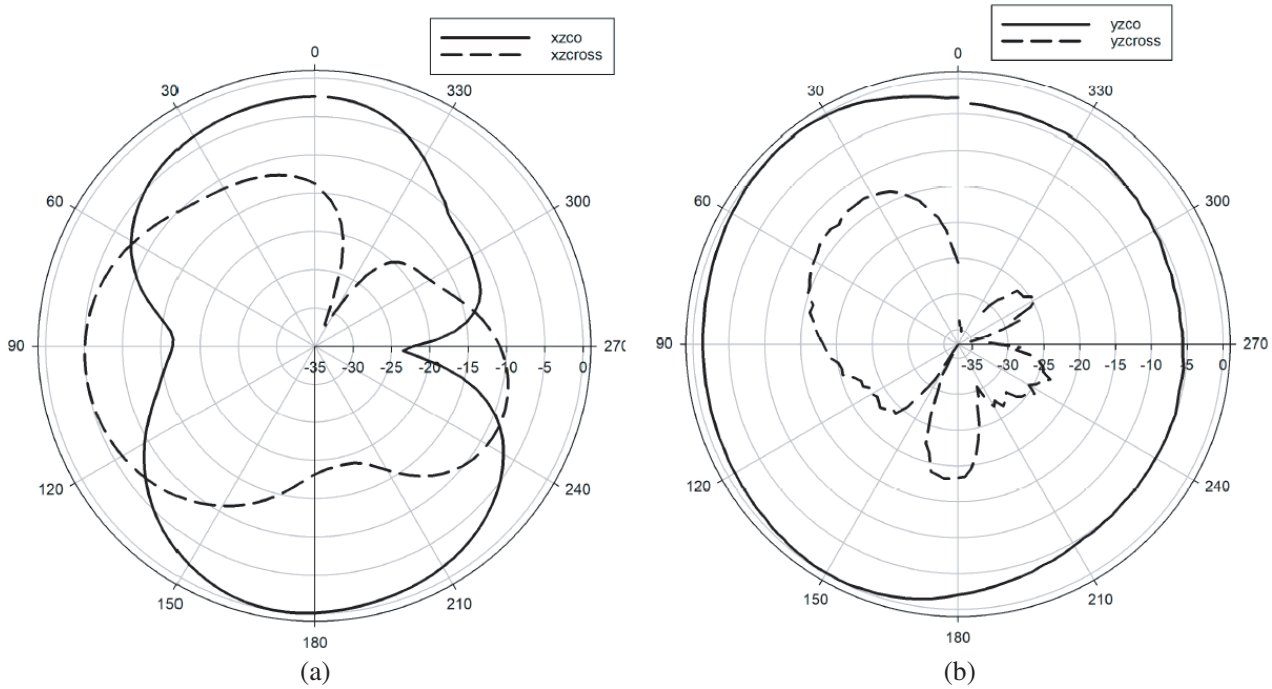

Figure 7. Co and cross polar radiation pattern. (a) XZ plane. (b) YZ plane.

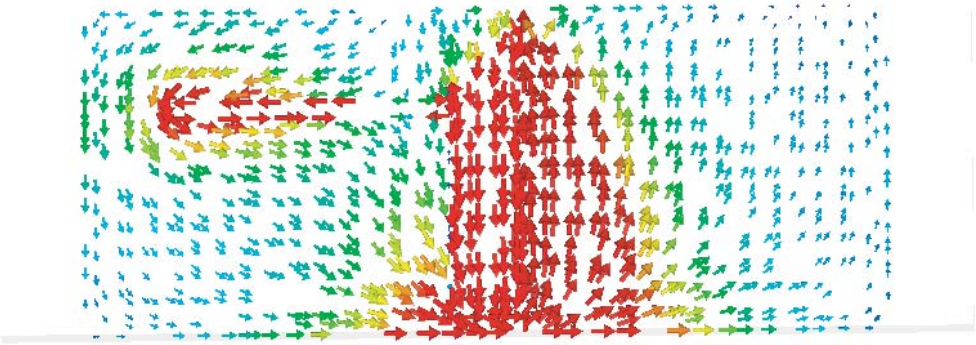

Figure 8. Surface current distribution of the reference antenna at resonance.

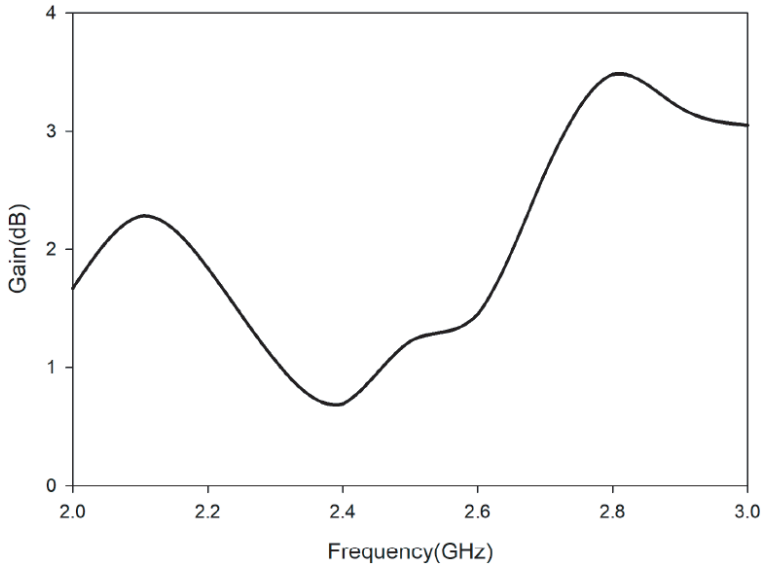

Figure 9. Measured gain of the reference antenna.

measured gain of the reference antenna is illustrated in Fig. 9. At the resonance frequency, a gain of 2.02 dB is observed. The simulated gain of the antenna as a function of frequency is also analyzed in the 2–3 GHz region. Initially, there is a decrease in gain with frequency. From 2.3 GHz onwards, there is an increase in gain with frequency. For the reference antenna an efficiency of 92.13% is obtained.

4.2. Antenna Loaded with Superstrate

A photograph of reference antenna loaded with superstrate is shown in Fig. 10.

When the antenna is loaded with superstrate, the periodic pattern with substrate provides a parasitic loading which results in improved matching. The bandwidth is not much affected by the presence of the superstrate. From the measured results, an impedance bandwidth of 374 MHz from 2.453 GHz to 2.827 GHz is observed for the antenna loaded with superstrate. In Fig. 11, a comparison of reflection characteristics of the reference antenna and the antenna loaded with superstrate is done. The variation in reflection characteristics with the variation in spacing between antenna and superstrate is shown in Fig. 12. It can be seen that neither the resonance frequency nor the magnitude of S_{11} is not much affected by the spacing variation.

It is well known that the gain of printed antennas can be improved by the use of a superstrate with proper parameters [2]. The gain can be further increased by printing periodic pattern on the

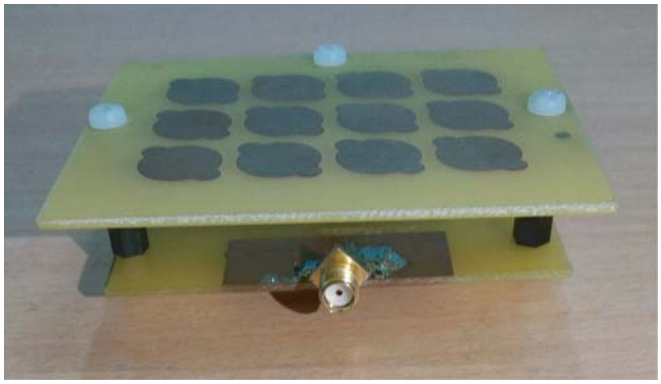

Figure 10. Antenna with superstrate.

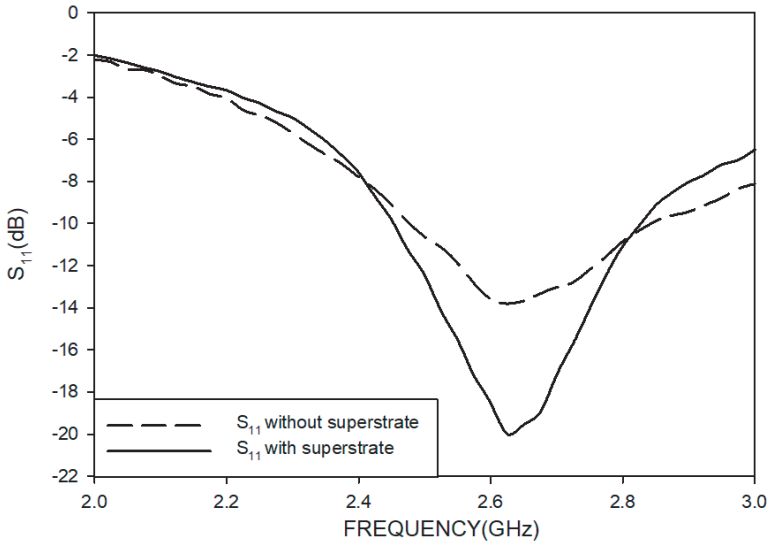

Figure 11. Reflection characteristics of reference antenna with and without superstrate.

superstrate. The simulation results show that the gain of the reference antenna is 1.96 dB at resonance frequency. The gain increases to 2.4 dB when a plain superstrate is used. When periodic pattern is printed on the superstrate, the gain further increases to 4.13 dB.

The measured gain of the reference antenna and the gain after adding the artificial dielectric superstrate are shown in Fig. 13. For the reference antenna at 2.65 GHz, a gain of 2.02 dB is observed. When the superstrate is added, the gain improves to 4.46 dB. At this frequency a high value of 18 is obtained for the effective permittivity of the artificial dielectric. Due to this high value of ϵ_r electric field confinement occurs which results in higher gain.

The gain is also a function of spacing between the antenna and the superstrate. The simulated results of variation in gain with respect to spacing is shown in Table 1. The optimum value of gain is obtained when the spacing is 20 mm.

The measured two-dimensional radiation patterns of the antenna with and without superstrate in XZ and YZ planes at 2.65 GHz for the co-polarization case are shown in Fig. 14. In the YZ plane the pattern is nearly omnidirectional, and a figure of 8 pattern is observed in the XZ plane. Comparing the radiation patterns with and without superstrate, the enhancement in gain can be clearly seen from the figure.

It can be seen that radiation patterns are more directive when the superstrate is added, as the superstrate directs the electromagnetic waves from the antenna towards boresight.

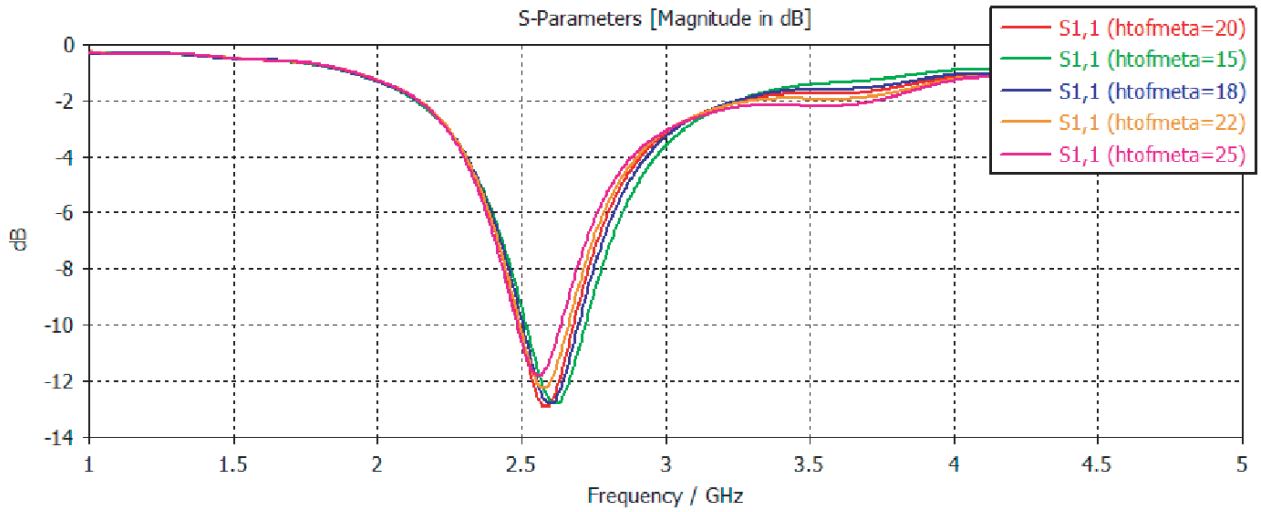

Figure 12. Variation of S_{11} with spacing between antenna and superstrate (htofmeta — spacing between antenna and superstrate).

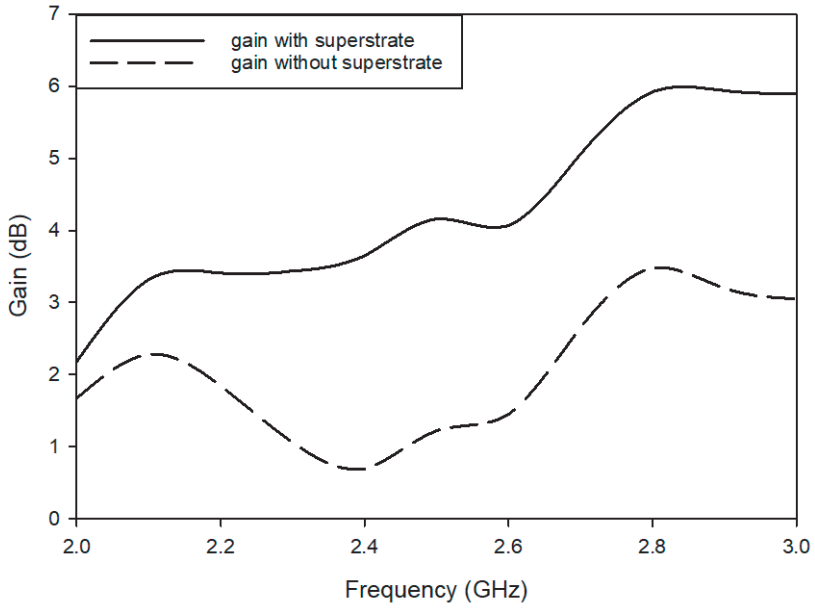

Figure 13. Measured gain of the reference antenna with and without superstrate.

Table 1. Variation of gain with spacing between antenna and superstrate.

Spacing between antenna and superstrate (mm)	gain (dB)
15	3.94
18	4.08
20	4.13
22	4.07
25	4.00

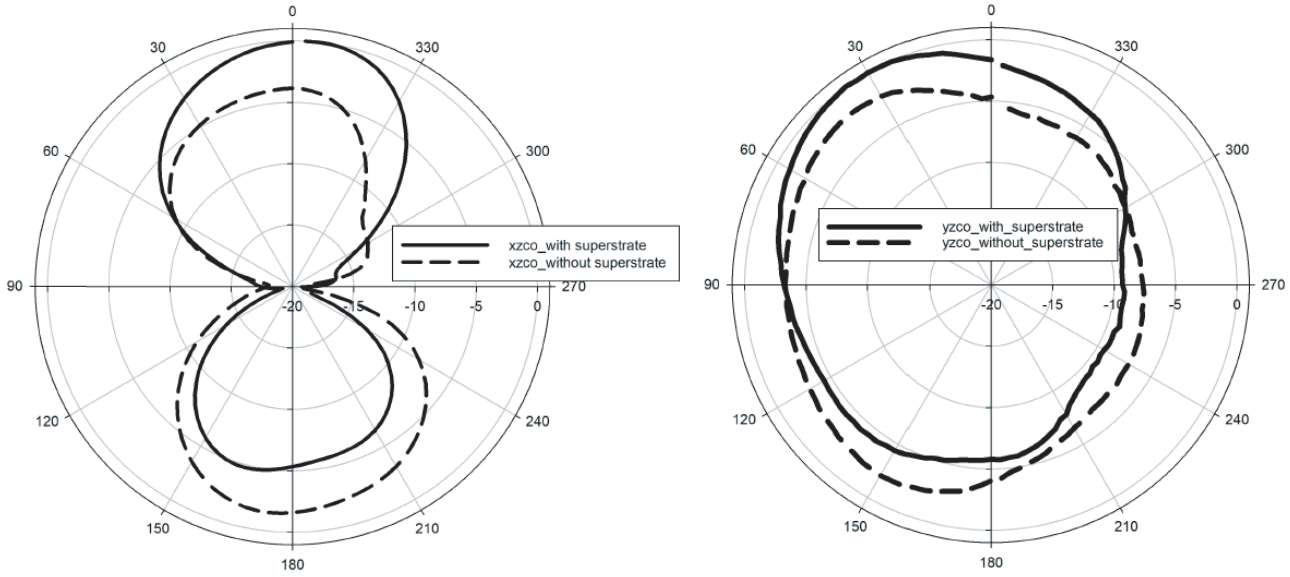

Figure 14. Measured two-dimensional co-polarization radiation pattern with and without superstrate for (a) XZ plane and (b) YZ plane.

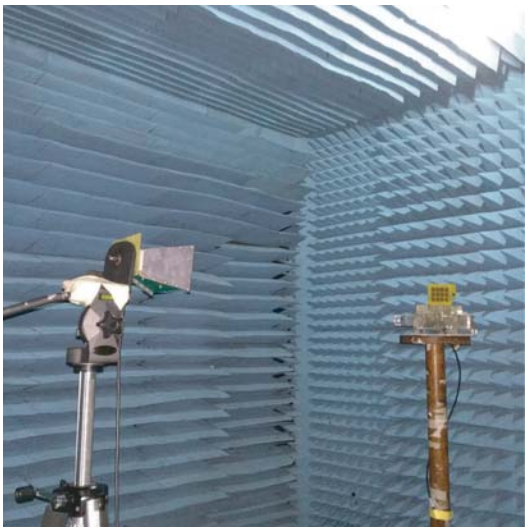

Figure 15. Radiation pattern measurement setup.

A photograph of the experimental setup for radiation pattern measurement is shown in Fig. 15.

5. CONCLUSION

In this paper, we have propose a technique for improving gain and impedance matching for a CPW-fed planar antenna. An artificial dielectric layer with a high value of effective permittivity is used as a superstrate. This artificial dielectric layer is formed by printing a finite size array of 3×4 unit cells on an FR-4 substrate. Compared with reference antenna, a gain enhancement of 2.50 dB is obtained when superstrate is used. The distance between the antenna and the superstrate is only $\lambda_0/6$ where λ_0 is the free space wavelength. Furthermore, the artificial superstrate helps in tilting the main beam towards boresight.

REFERENCES

1. Alexopoulos, N. and D. Jackson, "Fundamental superstrate (cover) effects on printed circuit antennas," *IEEE Transactions on Antennas and Propagation*, Vol. 32, No. 8, 807–816, 1984.
2. Jackson, D. and N. Alexopoulos, "Gain enhancement methods for printed circuit antennas," *IEEE Transactions on Antennas and Propagation*, Vol. 33, No. 9, 976–987, 1985.
3. Mittra, R., Y. Li, and K. Yoo, "A comparative study of directivity enhancement of microstrip patch antennas with using three different superstrates," *Microwave and Optical Technology Letters*, Vol. 52, No. 2, 327–330, 2010.
4. Ge, Y., K. P. Esselle, and Y. Hao, "Design of low-profile high-gain EBG resonator antennas using a genetic algorithm," *IEEE Antennas and Wireless Propagation Letters*, Vol. 6, 480–483, 2007.
5. Lee, Y. J., J. Yeo, R. Mittra, and W. S. Park, "Application of Electromagnetic Bandgap (EBG) superstrates with controllable defects for a class of patch antennas as spatial angular filters," *IEEE Transactions on Antennas and Propagation*, Vol. 53, No. 1, 224–235, 2005.
6. Chaimool, S., K. L. Chung, and P. Akkaraekthalin, "Simultaneous gain and bandwidths enhancement of a single-feed circularly polarized microstrip patch antenna using a metamaterial reflective surface," *Progress In Electromagnatics research B*, Vol. 22, 23–37, 2010.
7. Shaw, T., D. Bhattacharjee, and D. Mitra, "Gain enhancement of slot antenna using zero-index metamaterial superstrate," *International Journal of RF and Microwave Computer-Aided Engineering*, Vol. 27, e21078, 2016.
8. Kim, J. H., C. Ahn, and J. Bang, "Antenna gain enhancement using a holey superstrate," *IEEE Transactions on Antennas and Propagation*, Vol. 64, No. 3, 1164–1167, 2016.
9. Attia, H., L. Yousefi, M. M. Bait-Suwailam, M. S. Boybay, and O. M. Ramahi, "Enhanced-gain microstrip antenna using engineered magnetic superstrates," *IEEE Antennas and Wireless Propagation Letters*, Vol. 8, 1198–1201, 2009.
10. Syed, W. H. and A. Neto, "Front-to-Back ratio enhancement of planar printed antennas by means of artificial dielectric layers," *IEEE Transactions on Antennas and Propagation*, Vol. 61, No. 11, 5408–5416, 2013.
11. Sarkhel, A. and S. R. Bhadra Chaudhuri, "Enhanced-gain printed slot antenna using an electric metasurface superstrate," *Applied Physics A*, Vol. 122, No. 10, 934, 2016.
12. Attia, H., O. Siddiqui, and O. Ramahi, "Beam tilting of single microstrip antenna using high permittivity superstrate," *Microwave and Optical Technology Letters*, Vol. 55, No. 7, 1657–1661, 2013.
13. Pirhadi, A., H. Bahrami, and J. Nasri, "Wideband high directive aperture coupled microstrip antenna design by using a FSS superstrate layer," *IEEE Transactions on Antennas and Propagation*, Vol. 60, No. 4, 2101–2106, 2012.
14. Chen, X., T. M. Grzegorczyk, B.-I. Wu, J. Pacheco, Jr. and J. A. Kong, "Robust method to retrieve the constitutive effective parameters of metamaterials," *Phys. Rev. E*, Vol. 70, No. 1, 016608, 2004.
15. Buell, K., H. Mosallaei, and K. Sarabandi, "A substrate for small patch antennas providing tunable miniaturization factors," *IEEE Transactions on Microwave Theory and Techniques*, Vol. 54, No. 1, 135–146, 2006.
16. Mukherjee, B., P. Patel, and J. Mukherjee, "A novel hemispherical dielectric resonator antenna with complementary split-ring-shaped slots and resonator for wideband and low cross-polar applications," *IEEE Antennas and Propagation Magazine*, Vol. 57, No. 1, 120–128, Feb. 2015.
17. Sinha, M., V. Killamsetty, and B. Mukherjee, "Near field analysis of RDRA loaded with split ring resonators superstrate," *Microwave and Optical Technology Letters*, Vol. 60, No. 2, 472–478, 2018.
18. Simons, R. N., *Coplanar Waveguide Cicuits, Components and Systems*, John Wiley and Sons, New York, 2001.

Research Article

Experimental realization of electromagnetic toroidal excitation for microwave applications

V. P. Sarin[1] · P. V. Vinesh[1] · Mani Manoj[2] · Aanandan Chandroth[2] · Mohanan Pezholil[2] · Vasudevan Kesavath[2]

Abstract
An experimental realization of resonant toroidal dipole excitation in the microwave regime is presented in this paper. The metasurface proposed herewith is an asymmetric double split-ring resonator exhibiting Fano-like resonance profile. One could observe that cascading the metasurface results in near-field transverse and longitudinal coupling creating dual-band toroidal moments on the structure. This planar scheme will simulate the development of enhanced light–matter interaction, electromagnetic wave slowdown and sensor design. Here we report the experimental realization of the phenomenon in the S-band frequencies, and the results are verified using multipole scattering analysis.

Keywords Asymmetric metasurface · Fano resonance · Toroidal metamaterials · Toroidal dipoles

1 Introduction

Recent research interest has been focused on the scattering studies of a special type of excitation known as toroidal dipoles in composite metamaterial structures. The classical electromagnetic theory accounts only the scattering from electric and magnetic dipoles in the multipole scattering formalism [1]. An electric dipole is created by the separation of positive and negative charges, whereas a magnetic dipole is generated by virtue of circulating currents on a composite. The simultaneous excitation of electric and magnetic dipoles is used to tailor both magnitude and phase of transmission/reflection coefficients from a metamaterial composite [2, 3]. Toroidal dipoles are exempted from classical multipole expansion theory and are caused due to the surface current circulating on a metallic torus along its meridians. Their excitation in the nuclear system was first reported by Zel'dovich [4]. The far-field scattering pattern of a toroidal dipole is indistinguishable from that of an electric dipole [5]. Recently, there has been an immense interest in the development of toroidal metamaterials for electromagnetic wave manipulations. Artificial media exhibiting strong toroidal excitation are used for the creation of electromagnetically induced resonant transparency [6, 7]. They can also be used for creating a negative refractive index medium [8]. In conventional artificial media, a careful design procedure must be followed to suppress the excitation of electric and magnetic dipoles and to enhance toroidal dipole response. One such 3D configuration is the split loop structures immersed in a dielectric medium [9]. Singh et al. used asymmetric mirrored double split-ring structure and a combination of the split ring with dogbone metalization to generate toroidal dipole resonances in planar media [10, 11]. A different configuration proposed by the same group achieves Fano resonance observed in electromagnetically induced transparency system in addition to the toroidal response [12]. Recently, toroidal metamaterials have been successfully used for sensing and switching applications [13, 14]. Both Fano resonance and toroidal response can also be simultaneously excited in a stacked configuration of asymmetric split-ring resonators [15]. Localized toroidal spoof

✉ V. P. Sarin, sarincrema@gmail.com | [1]Department of Electronics, Government College Chittur, Palakkad, Kerala 678104, India. [2]Department of Electronics, Centre for Research in Electromagnetics and Antennas, Cochin University of Science and Technology, Cochin, Kerala 682022, India.

SN Applied Sciences (2019) 1:936 | https://doi.org/10.1007/s42452-019-0980-8

Received: 18 May 2019 / Accepted: 23 July 2019

Published online: 29 July 2019

plasmon polaritons are observed in split-ring resonators arranged in cylindrical fashion at microwave frequencies [16]. All dielectric metamaterials also support toroidal dipole excitation [17]. Dong et. al performed a variety of studies on toroidal dipole excitation in the microwave and THz regime [18–20]. Electromagnetic toroidal excitations in nature and artificial metamaterials are well reviewed in the literature [21]. An interesting application of toroidal metamaterials is the ease of creation of electromagnetic cloaks. It is worth mentioning that simultaneous excitation of electric and toroidal resonances could reduce the scattering cross section of the target [22–24]. The combination of both toroidal and dipole resonances is popularly known as an anapole. An anapole resonance is characterized by a strong electromagnetic energy concentration in the near field, and hence, it can be used for energy localization [25, 26]. Recently, toroidal resonators composed of water have been effectively used for achieving electromagnetic invisibility [27]. It is interesting to observe that dual-band toroidal response could be achieved by using a single array metasurface composed of trimmer clusters of high index dielectric cylinders [28]. It focuses on inter-cluster and intra-cluster coupling between neighboring particles to achieve dual-band response.

In this paper, the authors propose the use of a novel metamaterial for realizing resonant toroidal modes in the microwave regime. The advantage of the proposed design is that only two identical cascaded layers are only required to excite toroidal dipole modes. Cascading the metasurface enables both inter-layer and intra-layer near-field coupling which creates dual-band toroidal dipole moments on the structure for normal incidence. The advantage is that the excited toroidal moment significantly improves magnetic field confinement for the Fano resonance resulting in high quality factor for the Fano resonant peak. Simulation studies used for the characterization of metamaterial have been performed using CST Microwave Studio platform, and experiments are conducted inside and anechoic chamber using PNA E8362B network analyzer.

2 Design of the metasurface

Evolution of the proposed metamaterial structure is shown in Fig. 1. The fundamental structure constitutes a symmetric double split-ring resonator exhibiting strong electric dipole resonance as shown in Fig. 1a. Creation of an asymmetry in the structure by varying the width of vertical right arm as shown in Fig. 1b creates a Fano-like resonant peak in the transmission spectrum. Two such asymmetric surfaces are cascaded to get the final metasurface shown in Fig. 1c. The inter-element thickness 'd_z' is optimized after running parametric simulations in CST Microwave Studio.

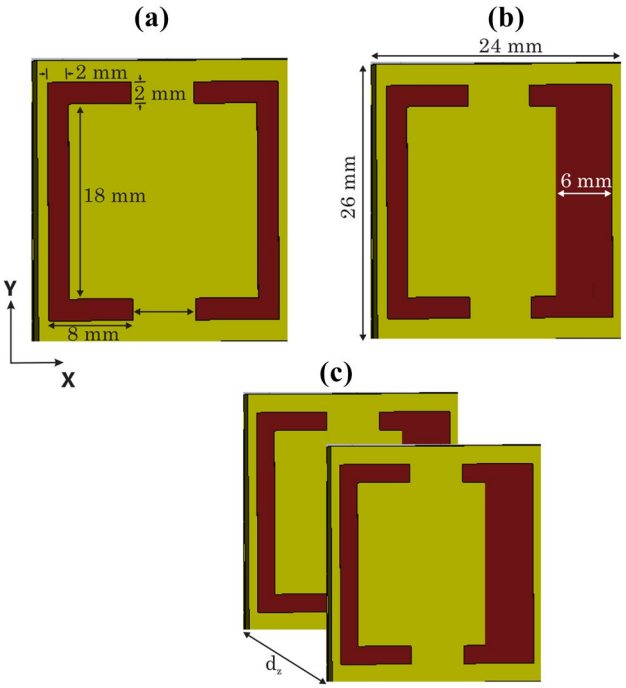

Fig. 1 Evolution of the metamaterial. **a** Symmetric double split-ring resonator, **b** asymmetric double split-ring resonator, and **c** stacked asymmetric double split-ring resonator

Unit cell parameters of the samples are indicated in the figure. The samples are fabricated using standard photolithographic manufacturing techniques. We used standard epoxy substrate having relative dielectric constant 4.4 and height 1.6 mm for fabrication. The array has a footprint of 210 mm × 300 mm, and two such arrays are cascaded using Perspex holders to yield the final design. The final fabricated structure is a 8 × 10 element array. Thickness of the printed copper metalization is 35 µm.

3 Characterization of the metamaterial

Unit cell simulations have been performed to retrieve the transmission spectra of the arrays for normal incidence. For that, periodic boundaries are applied on the top, bottom, left and right faces of the unit cell and frequency domain simulations have been performed using Floquet port excitation in CST Microwave Studio. Measurements have been performed inside an anechoic chamber using two ultrawideband horn antennas configured in transmission and reception mode. Initially, a THRU calibration is made with antenna separation held at 2 mm. Then the samples are placed in between the antennas in such a way that the electric field of the emitted radiation is made parallel to the metallic strip along *Y*-direction and resultant transmission spectra are measured for normal incidence.

An overview of the measured and simulated transmission spectra of the initial configuration shown in Fig. 1a is depicted in Fig. 2. The simulation and measurement are showing excellent agreement with each other. The reflective resonance at 3.37 GHz is characterized by a strong contribution from electric dipole excitation, and correspondingly, the transmission coefficient is extremely weak. Computed surface current distribution at resonance is depicted in Fig. 2b. Two symmetric half-wavelength resonant distributions with a current minimum at the open ends and maximum at the center are observed on each plate. This confirms the presence of an electric dipole moment P_y excited on the composite.

Transmission measurements are repeated for the asymmetric single layer structure shown in Fig. 1b, and the corresponding transmission spectrum is illustrated in Fig. 3. Introducing an asymmetry in the structure creates a tunnel band centered at 3.23 GHz as shown in Fig. 3a. Near-unity transmission is observed for this resonance. Excitation of electric dipole resonance is characterized by a dip in transmission coefficient at 3.1 GHz. The reason behind this newly introduced pass band resonance can be studied by verifying the surface currents excited on the structure as shown in Fig. 3b. As shown, the passband is caused due to the circular loop current distribution excited on the composite. This Fano-like resonance profile is contributed due to the simultaneous excitation of electric and magnetic moments on the structure. The circular

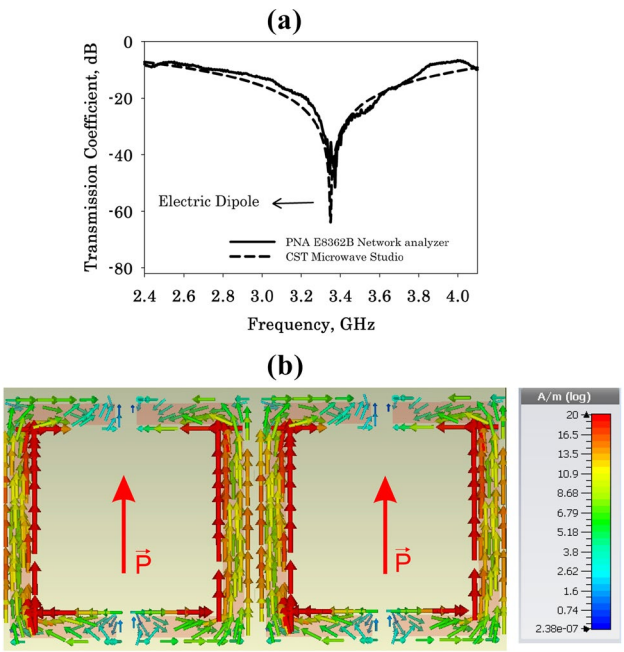

Fig. 2 Characterization of the symmetric unit cell. **a** Transmission spectrum and **b** surface current distribution at resonance

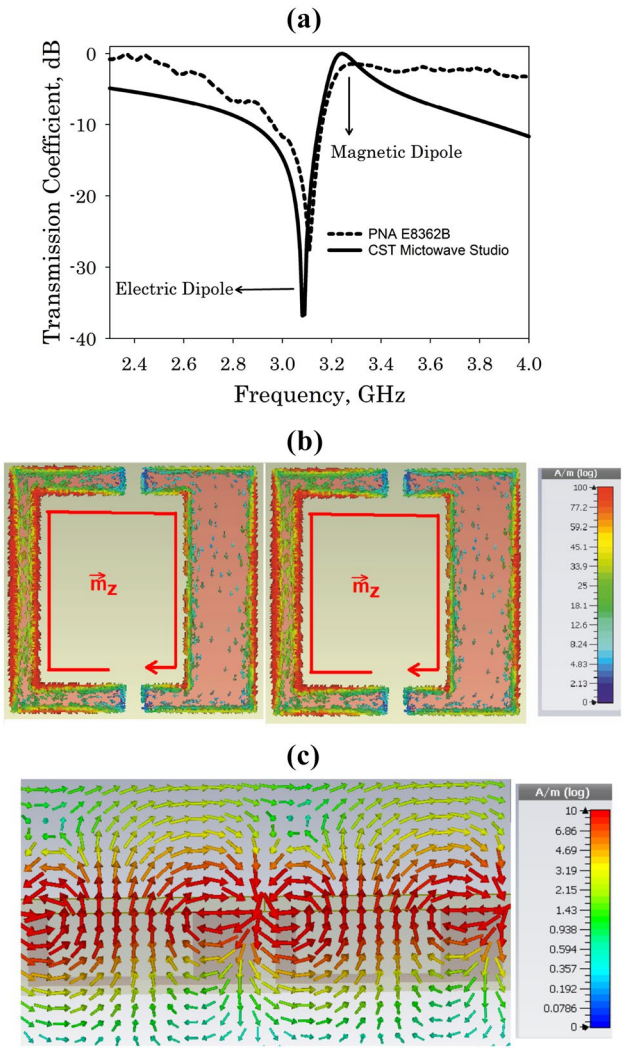

Fig. 3 Characterization of the asymmetric single layer metamaterial. **a** Transmission coefficient, **b** simulated surface current distribution at 3.23 GHz and **c** simulated magnetic field profile at 3.23 GHz

loop current excited on the *XY* plane of the metasurface creates a magnetic moment (M_z) on the composite. All the elements lying in the plane are excited in phase, and hence, magnetic moments on each loop will be oscillating in phase. Figure 3c illustrates the magnetic field intensity distribution in a plane perpendicular to the array. It is obvious that the resonant magnetic fields at the center of two consecutive elements are in phase. The Q-factor of this resonance is found to be 19 in simulation.

The final stacked metasurface depicted in Fig. 1c is assembled by fixing Perspex spacers in between the arrays for mechanical support. Figure 4 illustrates the transmission spectra of this stacked asymmetric composite for $d_z = 4.5$ mm. The structure shows two resonances for the band of interest as illustrated in the figure. The first resonance is found to be at 2.6 GHz, and the second one is at

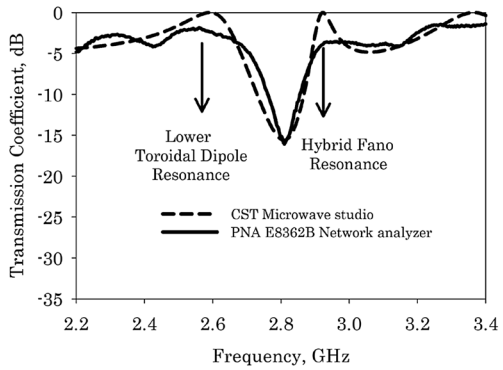

Fig. 4 Transmission coefficients of the stacked asymmetric metasurface

2.92 GHz. The electric dipole resonant dip is found to be at 2.8 GHz, and correspondingly, the transmission coefficient is very low of the order of − 16 dB. The slight mismatches between measurement and simulation are due to measurement tolerances. Q-factors of these resonances are found to be 10 and 41, respectively, in simulation. It is interesting to note that the quality factor for the second resonance is significantly enhanced. The first resonance is identified as the toroidal dipole resonance, and the second one is the hybrid Fano resonance. These conclusions are reached after performing multipole scattering analysis of the unit cell.

4 Multipolar scattering studies

Multipole scattering theory has been utilized to study the resonant mechanism of the final structure for $d_z = 5.5$ mm. Radiating power from the induced multipoles can be calculated by integrating the spatially distributed current distribution over the unit cell. The multipole amplitudes can be calculated as [5]

$$P = \frac{1}{i\omega}\int J\mathrm{d}^3 r \tag{1}$$

$$M = \frac{1}{i\omega}\int [\vec{r}Xj]\mathrm{d}^3 r \tag{2}$$

$$T = \frac{1}{10c}\int [(\vec{r}\cdot\vec{j})r - 2r^2 J]\mathrm{d}^3 r \tag{3}$$

where P is the electric dipole moment, M is the magnetic dipole moment, T is the toroidal moment, c is the velocity of light in vacuum, $\vec{r}$ is the displacement vector from the origin, ω is the angular frequency and J is the surface current density retrieved from simulations. The total power

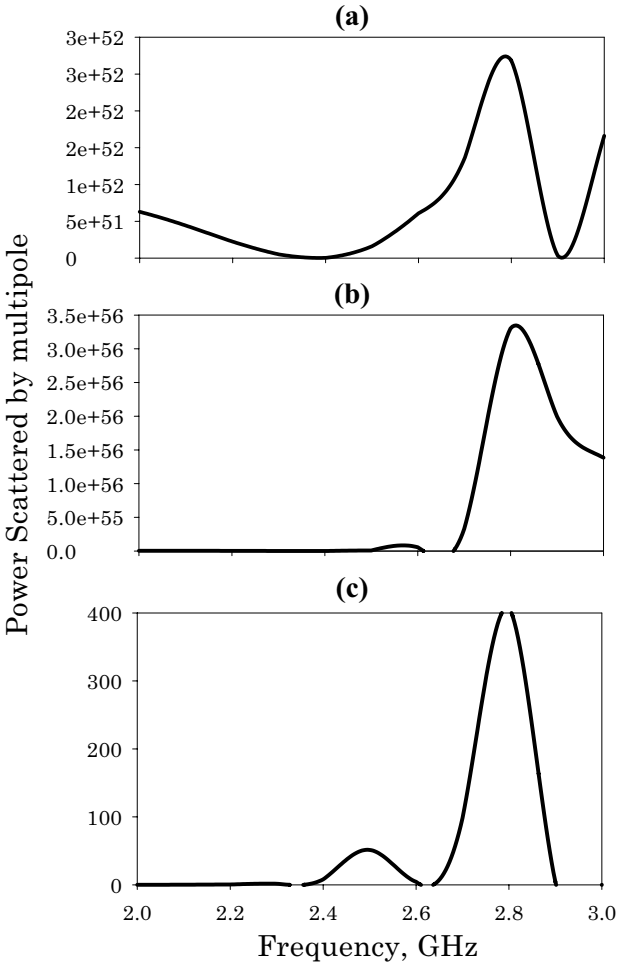

Fig. 5 Power radiated by multipoles. **a** Power radiated by electric dipole (P_y), **b** power radiated by magnetic dipole (M_z) and **c** power radiated by toroidal dipole (T_y)

radiated from different multipole moments can be formulated as

$$I = \frac{2\omega^4}{3c^3}\mid P\mid^2 + \frac{2\omega^4}{3c^3}\mid M\mid^2 + \frac{2\omega^6}{3c^5}\mid T\mid^2 + \cdots \tag{4}$$

Corresponding scattered power from the electric, magnetic and toroidal moments for the final structure is shown in Fig. 5. It is seen that the electric dipole moment P_y has a significant contribution throughout the full range of frequencies. The toroidal dipole T_y has a significant contribution for the lower resonance centered at 2.54 GHz in which the power radiated from the electric dipole moment is showing a significant dip. This dip is caused due to the scattering cancelation from anti-symmetric current distribution from stacked elements. Electromagnetic transmission is achieved by the virtue of the toroidal moment T_y on the composite. The presence of toroidal moment interferes destructively giving the lower transmission

peak at this resonance. The second resonance at 2.87 GHz is contributed by the combined effect of electric dipole P_y, toroidal dipole T_y and magnetic dipole M_z and hence can be named as the hybrid Fano resonance. The presence of magnetic and toroidal dipoles reduces reflection from the electric dipole moment giving near-unity transmission at this frequency. We have also performed the multipole scattering analysis of the asymmetric single layer structure depicted in Fig. 1b. It is noted that in that case, the contribution from the toroidal term is absent and resonance is contributed due to the simultaneous excitation of electric and magnetic dipole moments as that observed in Fano resonance-based transparency windows.

In order to verify the presence of toroidal excitation on the structure, the simulated magnetic field distributions in the *XZ* computational domain for the two resonances are taken into consideration and are shown in Fig. 6. In the simulation, the wave is propagating along + *Z* direction and the structure lies in the *XY* plane. It is observed that for the lower resonance at 2.54 GHz, the magnetic moments excited on two consecutive stacked elements are out of phase and it enables transverse intra-layer coupling. The resulting magnetic vortex formed in between the adjacent asymmetric arms creates toroidal dipole polarization T_y on the composite. The surface currents on the stacked plates will be out of phase at this frequency. The toroidal moment T_y excited on each cell is oscillating in phase

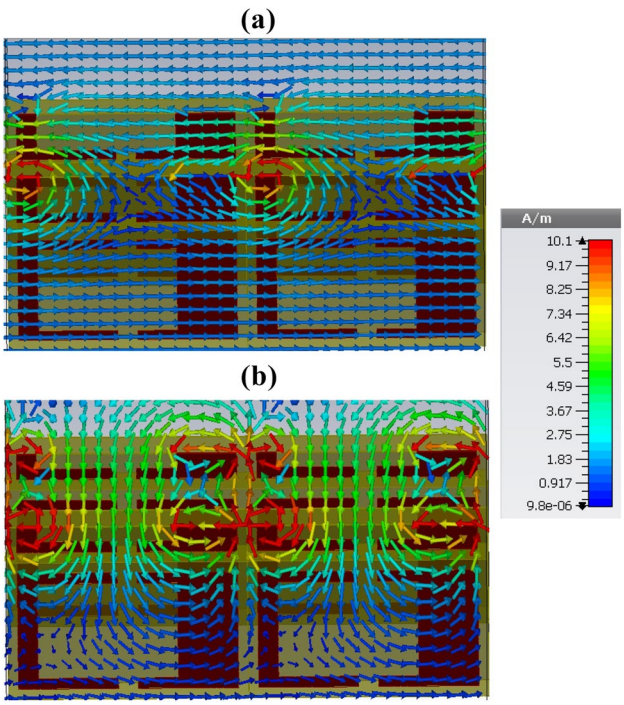

Fig. 6 Simulated magnetic field distributions at **a** 2.6 GHz and **b** 2.92 GHz

resulting in a transmission tunnel band. The higher resonance at 2.87 GHz shown in Fig. 6b is found to be hybrid in nature. It is interesting to note that toroidal dipole moment T_y is excited here by the longitudinal inter-layer coupling between the symmetric arms along the direction of propagation. The magnetic dipole moment M_z excited on the consecutive arms will be in phase and is verified by the presence of a longitudinal component of magnetic fields in between the loops. The peculiarity of the design is that stacking results in the creation of an additional toroidal moment for the Fano resonance which significantly modifies the field pattern. The fields are distributed on both the substrate and metallic parts which gives a high field localization within the unit cell. The excitation of this toroidal moment significantly improves the quality factor of second resonance. The enhanced magnetic field circulation around the metallic parts indicates the presence of enhanced toroidal dipole moment for this resonance as compared to the first resonance. The magnetic field distribution is highly localized for the second resonance in comparison with that of the single layer asymmetric structure. The enhanced toroidal excitation for the second resonance significantly enhances the Q-factor of the resonance as compared to the single layer Fano resonance structure. The presence of toroidal excitation is clearly seen in Fig. 5b as longitudinal coupling which is usually absent in conventional metamaterials exhibiting Fano resonances [15]. This gives the opportunity for an additional degree of freedom for controlling electromagnetic wave propagation. In high index dielectric particle-based configuration [28]; only transverse coupling within a layer is used to create dual-band response. This is due to the fact that coupling is achieved by the virtue of displacement currents. This type of dual-band in-plane coupling is practically impossible for asymmetric metasurface containing metallic implants. This is because of the fact that the proposed metasurface, containing metallic implants as the unit cell, works on the basis of conduction current. In these structures, intra-layer coupling by implementing cascading is the only possibility for the creation of an additional resonant toroidal mode.

5 Parametric analysis

A detailed parametric analysis has been performed in CST Microwave Studio to find out the effect of different structural parameters on metamaterial resonances. Figure 7 illustrates the effect of loading height h_1 in the transmission coefficient of the structure for normal incidence. It is observed that for a lower loading height ($h_1 = 0.5$ mm), a single resonant transmission peak of 2.7 GHz is observed which is due to the combined effect of toroidal, electric and magnetic dipoles. Increasing loading height splits this

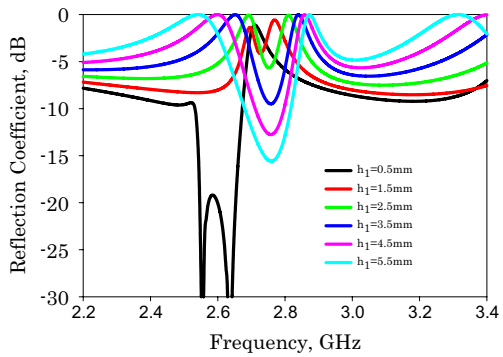

Fig. 7 Effect of stacking height on transmission characteristics

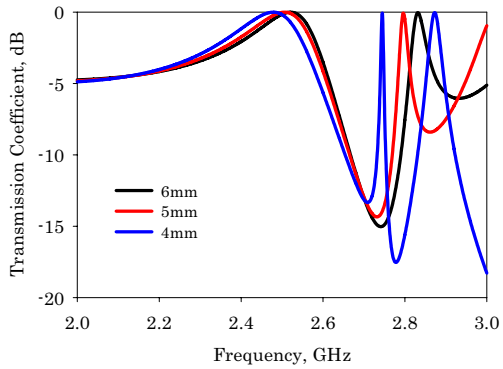

Fig. 8 Effect of asymmetry on transmission coefficient

resonance into two, and as the loading height is increased, the two resonances are found to shift toward opposite sides. The lower shifted resonance is identified as the toroidal resonance, and the higher shifted one is identified as the hybrid resonance of the composite. These conclusions are finalized from the multipolar scattering studies, and the results of such studies are omitted here for brevity.

We have also studied the effect of asymmetry on the transmission coefficient of the composite, and these results are illustrated in Fig. 8. Here the horizontal parameter of the asymmetric arm is varied in simulations. It is seen that decreasing the value of horizontal metalization slightly shifts the toroidal resonance to higher frequencies. But this variation is negligibly small. A significant lower shift is observed for the hybrid resonance. Higher asymmetry results in lower quality factor for the hybrid resonance.

6 Conclusions

An experimental realization of toroidal metamaterial in the microwave S-band frequencies is proposed in this study. The toroidal metamaterial constitutes a stacked asymmetric double split-ring resonator array printed on a low-cost epoxy substrate. It is worth mentioning that cascading the metasurface results in both transverse and longitudinal magnetic couplings resulting in dual-band toroidal response. It is noted that the presence of toroidal moment significantly enhances the quality factor of the Fano resonant transmission peak. The stacking thickness plays a crucial role behind the spectral separation and is optimized using computer simulations. Magnetic field map and multipole scattering theory reveal the excitation of dual-band toroidal moments in the composite under plane wave incidence.

Funding The authors acknowledge the financial support received from Department of Science and Technology (DST), Government of India, for the Project ECR/2017/002204.

Compliance with ethical standards

Conflict of interest The authors declare that they have no conflicts of interest.

References

1. Jackson JD (1999) Classical electrodynamics, 3rd edn. Wiley, Hoboken
2. Zhu BO, Zhao J, Feng Y (2013) Active impedance metasurface with full 3600 reflection phase tuning. Nat Sci Rep 49:1–6
3. Zhu BO, Chen K, Jia N, Sun L, Zhao J, Jiang T, Feng Y (2014) Dynamic control of electromagnetic wave propagation with the equivalent principle inspired tunable metasurface. Nat Sci Rep 4:1–7
4. Zel'dovich IB (1958) The relation between decay asymmetry and dipole moment of elementary particles. Sov Phys JETP 6:1184
5. Afanasiev GN, Stepanovsky YP (1995) The electromagnetic field of elementary time-dependent toroidal sources. J Phys A Math Gen 28:4565
6. Guo L-Y, Li M-H, Huang X-J, Yang H-L (2014) Electric toroidal metamaterial for resonant transparency and circular cross-polarization conversion. Appl Phys Lett 105:033507
7. Fedotov VA, Rogacheva AV, Savinov V, Tsai DP, Zheludev NI (2013) Resonant transparency and non-trivial non-radiating excitations in toroidal metamaterials. Nat Sci Rep 3:2967
8. Marinov K, Boardman AD, Fedotov VA, Zheludev N (2007) Toroidal metamaterial. New J Phys 9:1–12
9. Kaelberer T, Fedotov VA, Papasimakis N, Tsai DP, Zheludev NI (2010) Toroidal dipolar response in a metamaterial. Science 330:1510–1512
10. Gupta M, Singh R (2016) Toroidal versus Fano resonances in high Q planar THz metamaterials. Adv Opt Mater 201600553:1–7
11. Gupta M, Savinov V, Xu N, Cong L, Dayal G, Shuang W, Zhang W, Zheludev NI, Singh R (2016) Sharp toroidal resonances in planar terahertz metasurfaces. Adv Mater 201601611:1–6
12. Han S, Cong L, Gao F, Singh R, Yang H (2016) Observation of Fano resonance and classical analog of electromagnetically induced transparency in toroidal metamaterials. Ann Phys (Berl) 528(352–357):2
13. Gupta M, Srivastava YK, Manjappa M, Singh R (2017) Sensing with toroidal metamaterial. Appl Phys Lett 110:121108

14. Gupta M, Srivastava YK, Singh R (2017) A toroidal metamaterial switch. Adv Mater 30:201704845
15. Fan Y, Wei Z, Li H, Chen H, Soukoulis CM (2013) Low-loss and high-Q planar metamaterial with toroidal moment. Phys Rev B 87:115417
16. Kim S-H, Oh SS, Kim K-J, Kim J-E, Park HY, Hess O, Kee C-S (2015) Sub-wavelength localization and toroidal dipole moment of spoof surface plasmon polaritons. Phys Rev B 91:035116
17. Tasolamprou AC, Tsilipakos O, Kafesaki M, Soukoulis CM, Economou EN (2016) Toroidal eigenmodes in all-dielectric metamolecules. Phys Rev B 94:205433
18. Dong Z-G, Ni P, Zhu J, Yin X, Zhang X (2012) Toroidal dipole response in a multifold double ring metamaterial. Opt Exp 20:13065
19. Dong Z-G, Zhu J, Rho J, Li J-Q, Lu C, Yin X, Zhang X (2012) Optical toroidal dipolar response by an asymmetric double-bar metamaterial. Appl Phys Lett 101:144105
20. Dong Z-G, Zhu J, Yin X, Li J, Lu C, Zhang X (2013) All-optical Hall effect by the dynamic toroidal moment in a cavity-based metamaterial. Phys Rev B 87:245429
21. Papasimakis N, Fedotov VA, Savinov V, Raybould TA, Zheludev NI (2016) Electromagnetic toroidal excitations in matter and free space. Nat Mater 15:263–271
22. Miroshnichenko AE, Evlyukhin AB, Yu YF, Bakker RM, Chipouline A, Kuznetsov AI, Luk'yanchuk B, Chichkov BN, Kivshar YS (2015) Nonradiating anapole modes in dielectric nanoparticles. Nat Commun 6:8069
23. Nemkov NA, Stenishchev IV, Basharin AA (2017) Nontrivial nonradiating all-dielectric anapole. Nat Sci Rep 7:1064
24. Basharin AA, Chuguevsky V, Volsky N, Kafesaki M, Economou EN (2017) Extremely high Q-factor metamaterials due to anapole excitation. Phys Rev B 95:035104
25. Wu PC, Liao CY, Savinov V, Chung TL, Chen WT, Huang Y-W, Wu PR, Chen Y-H, Liu A-Q, Zheludev NI, Tsai DP (2018) Optical anapole metamaterial. ACS Nano 12:1920–1927
26. Ospanova AK, Labate G, Matekovits L, Basharin AA (2018) Multipolar passive cloaking by nonradiating anapole excitation. Nat Sci Rep 8:12514
27. Stenishchev IV, Basharin AA (2017) Toroidal response in all-dielectric metamaterials based on water. Nat Sci Rep 7:9468
28. Su X, Sayanskiy A, Kupriianov AS, Tuz VR, Kapitanova P, Sun H-B, Han W, Kivshar YS (2018) Experimental observation of toroidal dipole modes in all-dielectric metasurface. Adv Opt Mater 801166:1–9

Applied Physics A (2019) 125:703
https://doi.org/10.1007/s00339-019-3001-2

Applied Physics A
Materials Science & Processing

A metasurface-based evanescent amplification and propagation conversion for enhancing radiation from an electrically small radiator

V. Pushpakaran Sarin[1] · P. V. Vinesh[1] · Manoj Mani[2] · Aanandan Chandroth[2] · Mohanan Pezholil[2] · Vasudevan Kesavath[2]

Received: 20 June 2019 / Accepted: 8 September 2019

Abstract
Achieving super-resolution beyond the diffraction limit is an intriguing research topic over the last century. In this paper, the split-ring resonator array-based evanescent amplification in the microwave regime is implemented for strongly enhancing radiation from an electrically small radiator. The electrically small radiator considered here is a chip inductor loaded open coplanar waveguide antenna. This weakly radiating source when placed in the vicinity of split-ring resonator array, it is seen that the radiated power could be greatly enhanced. The split-ring resonator array working under the magnetic resonant excitation could amplify evanescent fields emitted by the source. Field probing reveals that the split-ring resonator array could convert the amplified evanescent waves into propagating ones resulting in significantly enhanced radiation from the source.

1 Introduction

Near-field imaging is a challenging and rapidly growing research topic over the last century. It is well known that the near-field of an electromagnetic source generates both propagating and evanescent waves. The former one carries real propagating power corresponding to the low spatial spectrum and it reaches the far-field. The later one, carrying sub-wavelength information about the source, carries reactive power and hence decays exponentially within the near-field of the source. This is the reason behind Abbe's diffraction limit in optical microscopy [1]. Several approaches have been proposed to date to overcome the diffraction limit in optical microscopes. Super-resolution beyond diffraction limit could be achieved by converting the reactive power into propagating ones. In optical near-field microscopes, sub-wavelength microsphere or an array of dielectric cylinders could be used for efficient spectral conversion [2, 3]. Recently, metamaterials have been effectively used for imaging beyond the diffraction limit. Metamaterials are artificial periodic inclusions which exhibit exotic material properties that are not available in nature [4, 5]. Pendry et al. showed that a negative index slab with material parameters $\varepsilon=\mu=-1$ could be used for evanescent amplification and could be used as a superlens [6]. But losses associated with this superlens deteriorate the performance of the system [7]. Anantha Ramakrishna et.al. proposed the use of a gain medium along with the lens to overcome this disadvantage [8]. The same group has achieved a refined superlens by cascading multiple negative index slabs [9]. Evanescent filtering using sub-wavelength gratings could also be used for near-field imaging [10]. The evanescent transport capability of such superlenses finds applications in optical lithography and sub-wavelength sensing [11]. Practical implementation of evanescent amplification is verified using transmission line metamaterials [12, 13], double planar resonant structures [14], etc. J.B Pendry also showed the possibility of the evanescent amplification based on epsilon-negative lens in the visible using a slab of Silver [6]. In the visible range, noble metals behave exactly like perfect plasma showing negative permittivity. In the microwave regime, the most possible method to implement evanescent amplification is to use a negative permeability medium. This important finding has been used in split-ring resonator-based wireless power transfer systems [15]. The main drawback of the near-field superlens is that after passing through the lens, evanescent wave emerging from the lens still undergoes exponential decay. To overcome this demerit, the far-field hyperlens concept has been introduced. Far-field superlens relies on converting the high spatial reactive spectrum existing near the source into a far-field propagating

✉ V. Pushpakaran Sarin
sarincrema@gmail.com

[1] Department of Electronics, Government College Chittur, Palakkad, Kerala 678104, India

[2] Department of Electronics, CREMA Lab, Cochin University of Science and Technology, Cochin, Kerala 682022, India

Published online: 17 September 2019

spectrum and could be collected with sensors located at the far-field [16]. A reverse process at the far-field could reconstruct the same near-field spatial distribution. The practical implementation of sub-wavelength metal strip grating-based reactive to propagation conversion for enhancing radiation from an electrically small antenna has also been validated [17]. The main drawback of sub-wavelength gratings is the one to many wave number mixing due to the simultaneous conversion to $n=0,+1$ and -1 spatial harmonics [18]. This could be overridden by carefully designing the transfer function of the transmission grating. Durant et. al. designed the first far-field hyperlens using a corrugated silver slab [19]. The silver slab could be used for evanescent amplification [20, 21] and the corrugations could convert the amplified high spatial reactive spectrum into low spatial one with one to one correspondence with the grating transfer function is so designed such that only the $n=-1$ spatial harmonic efficiently radiates.

The authors proposed the use of sub-wavelength metal strip gratings for enhancing radiation performance of an electrically small antenna (ESA) [22]. The sub-wavelength metal strip grating efficiently converts the high spatial reactive spectrum into low spatial propagating ones. In this paper, the split-ring resonator array-based evanescent amplification is implemented for enhancing radiation performance of the electrically small dipole source. The advantage of the proposed configuration is that the split-ring resonator array not only amplifies the evanescent near-field spectrum but also converts these evanescent waves into propagating ones resulting in significantly enhanced radiation performance. Computational studies of the proposed design are performed using CST Microwave Studio and experiments are performed inside an anechoic chamber using PNA E8362B vector network analyzer.

2 Results and discussion

2.1 Characterization of the split-ring resonator array

The split-ring resonator array is a good candidate for achieving mu negative bandgap at its resonant frequency. A split-ring resonator array working under $H_{||}$ excitation can be approximated as an anisotropic medium characterized by an effective permeability given by [23]

$$\mu = \mu_0\left(1 - \frac{f_p^2}{f^2 - f_0^2}\right) \tag{1}$$

where f_p is the plasma frequency, the resonant frequency $f_0 >> f$p and μ_0 is the permeability of free space. It is evident from the equation that effective permeability offered by the medium is negative above resonant frequency f_0. The selected split-ring resonator array is characterized using simulations in CST Microwave Studio and its geometrical specifications and characteristics are depicted in Fig. 1. Effective parameters are retrieved in simulations by assigning waveguide ports such that the incident electric field is oriented parallel to the slits and magnetic field parallel to the axis of the split-ring resonator as shown in Fig. 1a. The dimensions of the SRR are $r=6.7$ mm, $d=2$ mm, $s=0.8$ mm, $w=1$ mm, $h=1.6$ mm and $p_1=p_2=20$ mm. Reflection and transmission coefficients of this split-ring resonator under this excitation scenario are depicted in Fig. 1b. The structure shows strong reflective resonance at 2.2 GHz and this resonance is attributed due to the excitation of magnetic resonance in the composite. Retrieved effective permittivity and permeability of the artificial medium are illustrated in Fig. 1c. It is clear that the structure shows permeability resonance and shows negative values of permeability after resonance. Permeability resonance indicates that the structure would offer a strong reflection for propagating electromagnetic waves resulting in a transmission dip at resonance. The situation becomes quite different for an evanescent source placed in front of an artificial permeability medium. In conventional systems, two techniques are used for the creation of an evanescent source. The first method is the use of wax prism technique, which utilizes a highly collimated microwave plane wave with the angle of incidence made higher than critical angle [24, 25]. The generated evanescent waves will resonantly couple to the surface Plasmon modes of the metamaterial resulting in transmission dip. The second method utilizes an evanescent waveguide whose dimensions are selected such that the selected frequency of operation is well below the cutoff [26]. Split-ring resonator well placed in such a waveguide system shows evanescent amplification.

2.2 Characterization of the electrically small radiator

It is well known that an electrically small radiator could be approximated as an evanescent source. The power radiated from an electrically small radiator can be approximated as [27]

$$P = \eta\left(\frac{\pi}{3}\right)\left|\frac{I_0}{\lambda}l\right|\left[1 - j\frac{1}{(kr)^3}\right], \tag{2}$$

where η is the wave impedance, I_o is the driving current, λ is the operating wavelength, l is the length of the antenna, k is the free space wavenumber and r is the distance from the center to the observation point. It is clear that this radiator has a large capacitive near-field power and hence the radiation efficiency will be poor. A reactive near-field indicates the presence of electric and magnetic fields which are spatially and temporally shifted in phase. In a capacitive

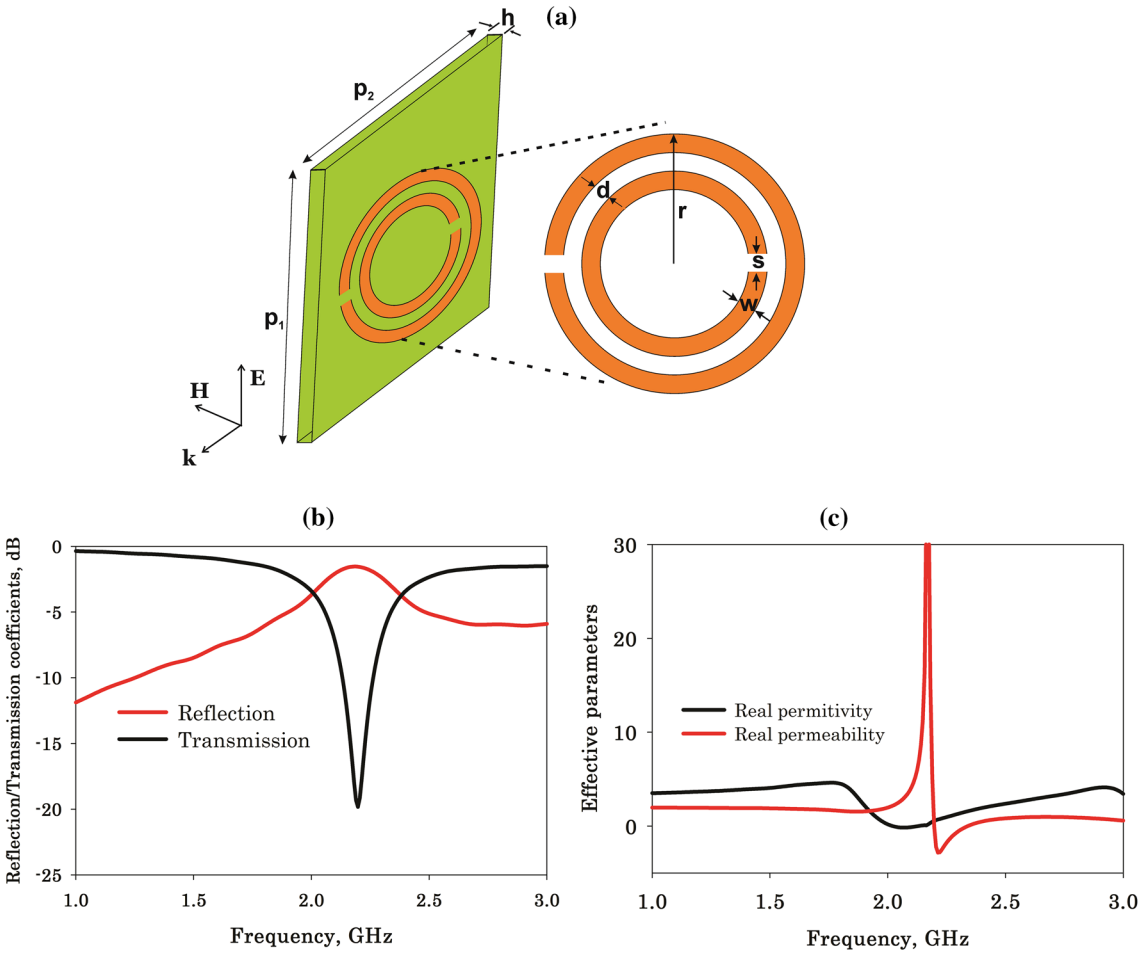

Fig. 1 Characterization of the split-ring resonator. **a** Geometric description of the unit cell, **b** reflection and transmission coefficients of the array and **c** retrieved material parameters

near-field, the electric field lags the magnetic field by a temporal phase shift. If this temporal phase shift is 90°, then it represents an ideal evanescent source and shows exponential decay along the direction of propagation. The novelty of the proposed work is that the selected electrically small antenna (ESA) acts as an evanescent source. The specialty of this radiator is that it is well-matched to free space showing resonance, but its near-field analysis predicts the presence of high spatial reactive spectrum in addition to the propagating far-field spectrum. Since the resonance of the selected ESA coalesces with the negative permeability region of the SRR array, the emitted evanescent waves get amplified which significantly enhances the radiation performance of the source.

To implement the technique, we selected the chip inductor-loaded open coplanar waveguide antenna as the radiator [28]. The peculiarity of this radiator is that it falls well below the Chu limit and is perfectly matched showing a reflection coefficient better than − 10 dB threshold level. The antenna uses a compact coplanar waveguide feed with a coil Craft chip inductor, having inductance 23 nH, soldered in between the center conductor and top rectangular metallization. It occupies an area of $0.08\lambda_0 \times 0.0479\lambda_0$ and at the resonant frequency; the ka value is 0.2924 which is much smaller than the Chu limit. The microwave signal is fed using a standard SMA connector soldered to the lower bottom end of the Coplanar Waveguide. Dimensions of the antenna are $P_g = 0.8$ mm, $P_w = 1$ mm, $P_h = 0.8$ mm, $L_g = 4$ mm, $W_g = 3$ mm. The ESA is fabricated on a low-cost Copper clad epoxy substrate of dielectric constant 4.4 and thickness $h = 1.6$ mm. Geometry and radiation characteristics of the antenna are depicted in Fig. 2.

Figure 2a shows the geometric specifications of the antenna and the fabricated prototype is depicted in Fig. 2b. The reflection coefficient of this antenna is depicted in Fig. 2c. As shown, resonance is found to be at 2.38 GHz and it shows a reflection coefficient value of − 12 dB in the experiment. The experiment and simulation are well matched. Resonant mechanism of this ESA is well understood by studying the simulated electric field distributions at resonance over the antenna aperture as depicted in the

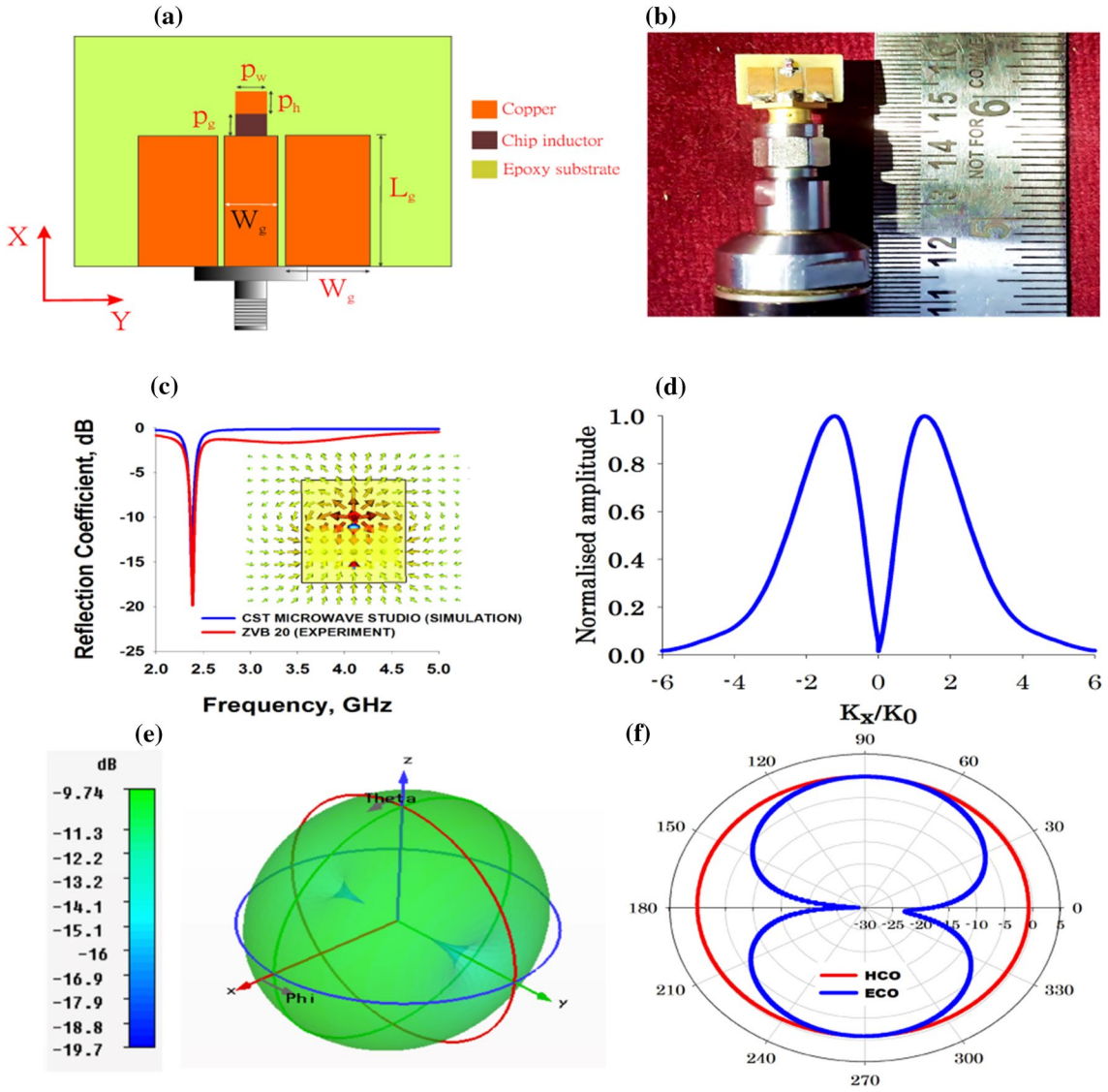

Fig. 2 Characterization of the ESA. **a** Geometric description, **b** photograph of the antenna, **c** reflection coefficient with the resonant electric field at the inset, **d** normalized radiated spectrum, **e** simulated 3D gain pattern and **f** principal plane radiation patterns

inset of Fig. 2c. It resembles the field pattern of a monopole excitation and emits vertically polarized radiation. As pointed out earlier, an ideal electrically small radiator is not perfectly matched due to the highly capacitive reactance and hence all the input power fed into its terminal would be reflected back. But here, a well-defined resonance curve is observed and to find the reason behind this, the near-field electric distribution emitted by the radiator is taken into consideration. Spatial Fourier transform operation is applied on the near-field electric field distribution and corresponding spatial spectrum emitted the source is depicted in Fig. 2d. The spectrum has been normalized with the maximum radiated power. Spectral components having spatial wave number $|K_x/K_0|<1$ are designated as the propagating spectrum causing far-field radiation. Spectral components with $|K_x/K_0|>1$ are referred to as reactive spectrum containing reactive power and will be available only in the near-field of the source. It is obvious that the propagating spectrum of the emitted radiation is significantly weak and the antenna near-field is dominated by the reactive spectrum. Due to this reason, the radiation efficiency of this antenna will be very low. Measured radiation efficiency calculated using the Wheeler Cap method is found to be only 13% at resonance. The simulated 3D radiation pattern of this radiator depicted in Fig. 2e shows omnidirectional radiation characteristics at resonance. The E-plane and H-plane radiation patterns in Fig. 2 f confirm uniform radiation coverage along H-plane and a dot nut-shaped pattern with radiation nulls along the antenna axis for E-plane.

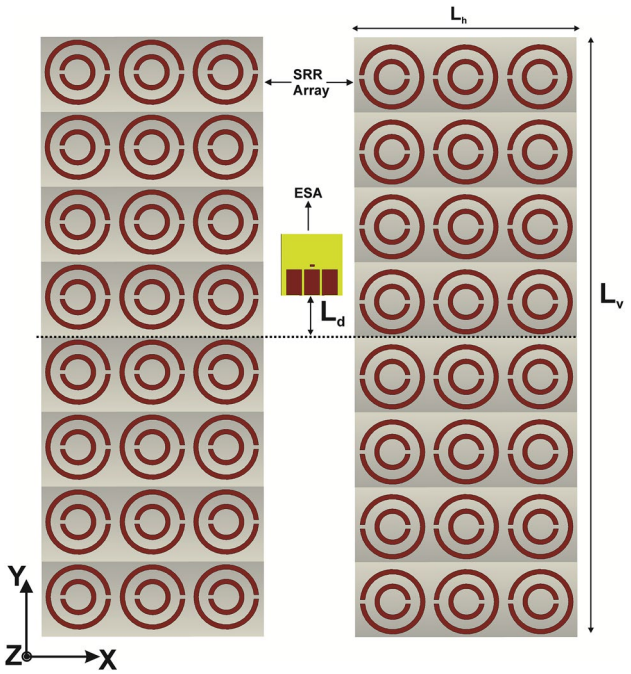

Fig. 3 Geometry of the split-ring resonator array-loaded electrically small antenna

2.3 Characterization of the SRR array-loaded ESA

Since the negative permeability region of the SRR covers the resonant frequency of the ESA, the antenna can be used as an evanescent source for the metamaterial. For that, we placed the ESA in between two planar arrays of SRR as depicted in Fig. 3. The geometry of the proposed SRR array loaded electrically small radiator is shown in Fig. 3. To excite magnetic resonance, the splits are arranged parallel to the radiated electric field of the reference antenna. Two 3×8 element SRR arrays, printed on an epoxy substrate of dielectric constant 4.4 and height 1.6 mm, are placed on both sides of the ESA such that the array on one side is exactly the mirror image with that on the other side. The dimensions of the single array are $L_h = 60$ mm and $L_v = 160$ mm. The antenna is placed asymmetrically along *Y*-direction such that the offset parameter from the center is $L_d = 2$ mm. Asymmetry enables maximum radiated power and is optimized after running parametric simulations in CST Microwave Studio. The antenna reference level is indicated with horizontal dotted black lines in the figure.

Effect of variation in the number of columns of SRR placed on both sides of the ESA has been studied in simulations and corresponding variations in gain patterns are formulated in Fig. 4. Figure 4a, b illustrates this variation for the two principal planes. The gain pattern of the ESA without the metamaterial layer is also included in the figure (black line) for comparison. It is interesting to observe that the metamaterial incorporated designs significantly improve power radiated from the ESA. The optimum design having three columns of SRR array on both sides of the ESA achieves maximum radiated power along the upper and lower hemisphere of the antenna. In simulations, the ESA without the metamaterial layer shows a radiated gain of − 8.5 dBi whereas the gain of the loaded configurations is

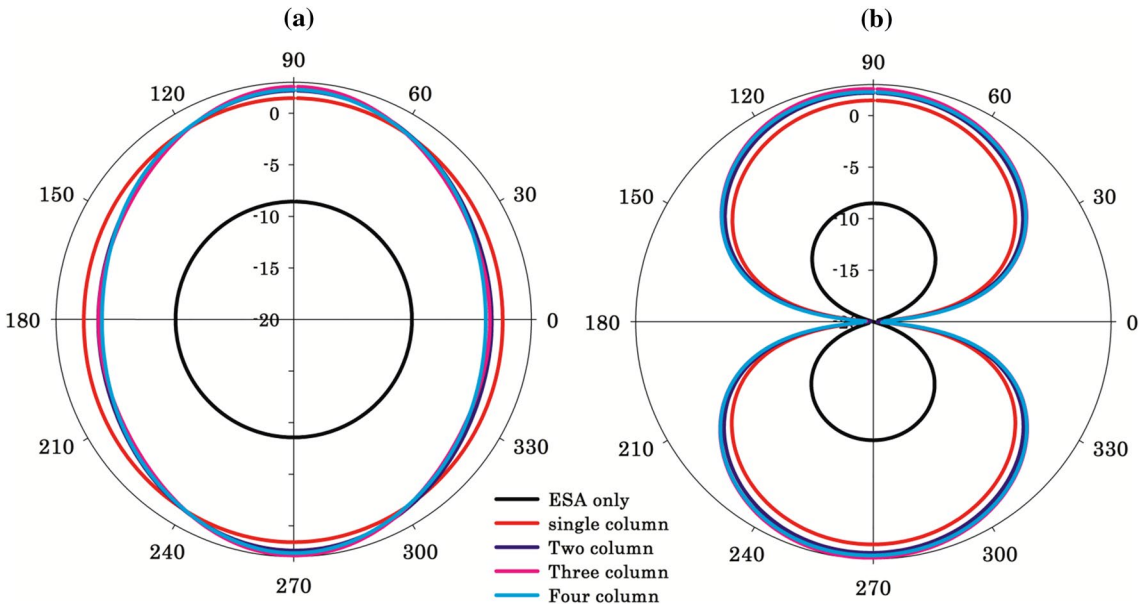

Fig. 4 Effect of variation in the number of columns of SRR on radiation characteristics **a** variation in H-plane pattern and **b** variation in E-plane pattern

significantly enhanced. The optimum design having three columns of SRR shows a gain of 2.5 dBi in simulation. We have also calculated the conductor losses associated with the antennas in CST simulations. It is to be noted that the conductor loss is maximum for the three-column case and is found to be only 2.8% in comparison with the total radiated power. If the resonance of the antenna is brought in close proximity with that of SRR resonance by changing the structural parameters, the conductor losses will be further increased.

To find the reason behind this peculiar radiation performance, the magnetic field distributions over the reference line indicated in Fig. 3 are computed at the resonant frequency using CST Microwave studio and these results are included in Fig. 5.

It is seen that for the single-column configuration (black line), the magnitude of the magnetic field shows exponential growth from the ESA location to the SRR location followed by an exponential decay. The magnetic field amplitude is enhanced from 0.01 to 0.05 A/m and this first peak is associated with the presence of the first SRR. It is noted that the decay from the first peak is not exponential for the last three cases. The successive peaks associated with each design indicate the presence of an SRR.

Two prototypes, one with single column and the second with three columns of SRR on both sides of the ESA, have been fabricated using photolithographic procedures and their performances are validated with measurements using PNA E8362B network analyzer inside an anechoic chamber. Reflection and radiation characteristics of these fabricated samples in comparison with the reference ESA are illustrated in Fig. 6. Figure 6a illustrates the reflection coefficients of these fabricated prototypes. It is noted that the resonant frequency remains unchanged for all these three configurations. An interesting fact is that radiated power from the SRR-incorporated designs is tremendously enhanced. This is verified by measuring transmission coefficients of these fabricated antennas and corresponding results are included in Fig. 6b. It is observed that maximum radiated power is observed for the three-column configuration and the radiated power is enhanced from – 61 to – 51 dB in comparison with the ESA without metamaterial. This implies that a tenfold enhancement in radiated power is observed at the observation point in comparison with that of the ESA without metamaterial. Radiation pattern measurements are performed inside an anechoic chamber by positioning the designed antennas in a turntable assembly. The antennas under test are rotated using the computer-controlled turntable assembly and the received powers are recorded in a computer system for both the principal planes. Measured principle plane radiation patterns of these designed prototypes are illustrated in Fig. 6c, d. 3 dB beamwidth for this configuration is found to be 40° for the E-plane and 73° for the H-plane. The gain of the antennas is measured using the standard gain comparison method. The measured gain is found to be 1.5 dBi at resonance. Photograph of the radiation pattern measurement setup is shown in Fig. 6e.

To verify the reason behind radiation enhancement, the electric field distributions along the line located 10 cm away from the antenna plane were taken into consideration. The spatial transform operation is then performed and the corresponding normalized spatial frequency spectrum radiated by the SRR-loaded antenna and the ESA in free space are illustrated in Fig. 7. It is observed that the spatial spectrum of the SRR-loaded design is narrower than that of the ESA in free space. The amplitude of spectral components for the SRR loaded design is enhanced as compared to that of ESA in free space. This enhancement is attributed due evanescent

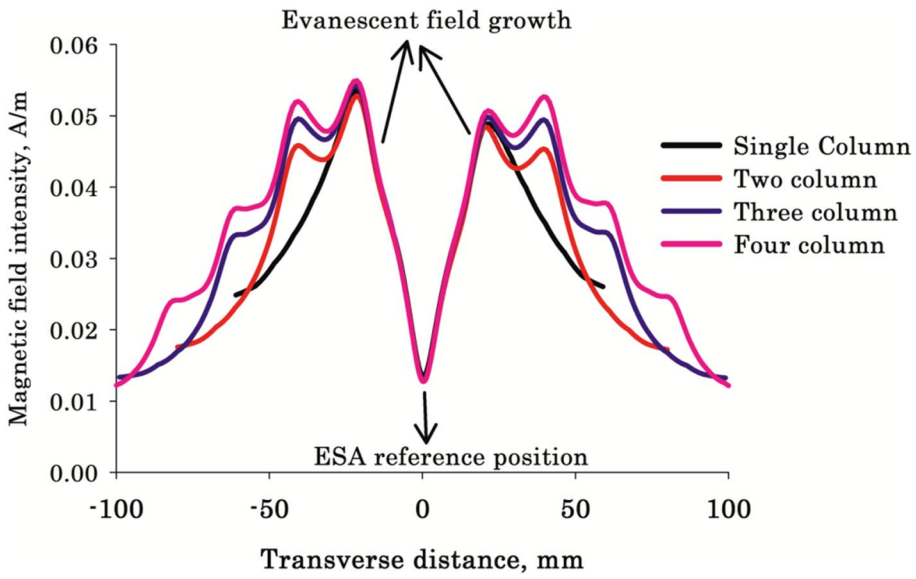

Fig. 5 Demonstration of evanescent field enhancement for different configurations

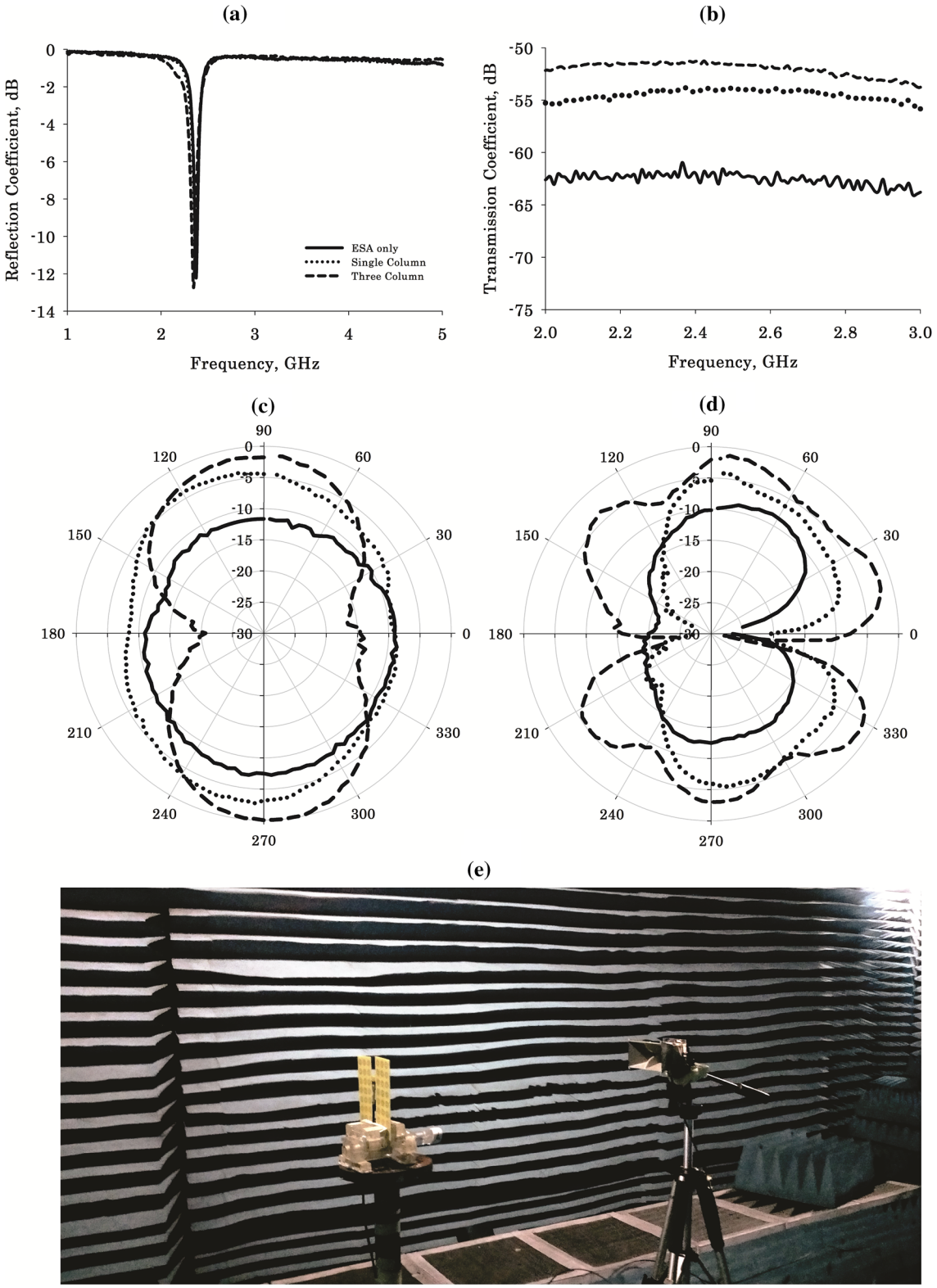

Fig. 6 Measurements on the fabricated prototypes. **a** Reflection coefficients of fabricated antennas, **b** comparison of radiated power captured by an ultra-wideband antenna located at far-field for the fabricated designs, **c** H-plane radiation patterns, **d** E-plane radiation patterns and **e** radiation pattern measurement setup

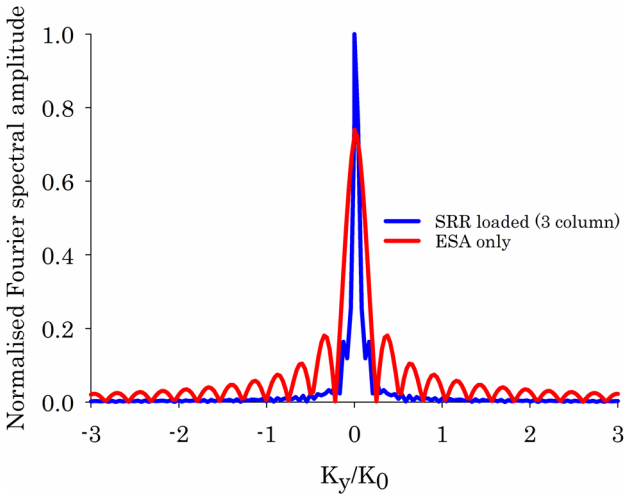

Fig. 7 Normalized Fourier spectral amplitudes radiated by the antennas

to propagation conversion offered by the split-ring resonator array. So it can be said that the SRR layer not only amplifies the evanescent waves in the near-field of the antenna but also converts these enhanced high spatial spectrum into low spatial ones. This conversion is responsible for enhanced radiation performance from the ESA. This condition is equivalent to the operation of the well known far-field hyperlens theory in which periodic gratings are responsible for evanescent to propagation conversion [18, 19]. It is to be noted that the conventional metamaterial lens antennas interact with the propagating spectrum of the emitted radiation to achieve beam focusing to yield high gain radiation patterns [29, 30].

3 Conclusions

Enhanced radiation performance of an electrically small antenna based on evanescent amplification using a split-ring resonator array in the microwave regime is physically realized in this paper. The electrically small antenna serves as an evanescent source for the split-ring resonator array and the source when placed in the vicinity of the metamaterial results in evanescent amplification. Field probing reveals that the split-ring resonator array converts the high spatial evanescent spectrum existing in the near-field into propagating spectrum resulting in enhanced radiation characteristics. It is observed that the gain of the antenna is enhanced to 1.5 dBi from − 8.5 dBi at resonance. Simulation results are validated using experiments with vector network analyzer inside an anechoic chamber. This technique will surely stimulate the development of enhanced range wireless power transfer system for microwave wireless charging applications.

Acknowledgements The authors acknowledge the research funding received from the Science and Engineering Research Board (SERB), Department of Science and Technology for the major research project ECR/2017/002204. The authors gratefully acknowledge the facilities and support given by Advanced Centre for Atmospheric Radar Research and DST PURSE scheme provided to Cochin University of Science and Technology by DST, Govt. of India.

References

1. M. Born, E. Wolf, *Principles of optics*, 7th edn. (Cambridge University Press, Cambridge, 1999)
2. P. Pawliuk, M. Yedlin, Evanescent wave impedance and scattering conversion into radiation. Appl. Phys. B **114**, 407 (2014)
3. Y. Ben-Aryeh, Transmission enhancement by conversion of evanescent to propagating waves. Appl. Phys. B Laser Opt. **91**, 157 (2008)
4. A. Alu, N. Engheta, A. Erentok, R.W. Ziolkowski, Single-negative double-negative and low-index metamaterials and their electromagnetic applications. IEEE Antennas Propag. Mag. **49**, 23 (2007)
5. N. Engheta, R. Ziolkowski, *Metamaterials: physics and engineering explorations* (Wiley-IEEE, New York, 2006)
6. J.B. Pendry, Negative refraction makes a perfect lens. Phys. Rev. Lett. **85**, 03 (2000)
7. G. D'Aguanno, N. Mattiucci, M.J. Bloemer, Influence of losses on the superresolution performances of an impedance-matched negative-index material. J. Opt. Soc. Am. B **25**, 236 (2008)
8. S.A. Ramakrishna, J.B. Pendry, Removal of absorption and increase in resolution in a near-field lens via optical gain. Phys. Rev. B **67**, 201101 (2003)
9. J.B. Pendry, S.A. Ramakrishna, Refining the perfect lens. Phys. B Cond. Matter. **338**, 329 (2003)
10. G. Fedorov, S.I. Maslowski, A.V. Dorofeenko, A.P. Vinogradov, I.A. Ryzhikov, S.A. Tretyakov, Subwavelength imaging: resolution enhancement using metal wire gratings. Phys. Rev. B **7**, 117 (2006)
11. X. Luo, T. Ishihara, Surface plasmon resonant interference nanolithography technique. Appl. Phys. Lett. **84**, 4780 (2004)
12. G.V. Eleftheriades, A.K. Iyer, P.C. Kremer, Planar negative refractive index media using periodically L-C loaded transmission lines. IEEE Trans. Antennas Propag. **50**, 2702 (2002)
13. A. Grbic, G.V. Eleftheriades, Overcoming the diffraction limit with a planar left-handed transmission-line lens. Phys. Rev. Lett. **92**, 117403 (2004)
14. S. Maslovski, S. Tretyakov, P. Alitalo, Near-field enhancement, and imaging in double planar polariton-resonant structures. J. Appl. Phys. **96**, 1293 (2004)
15. B. Wang, K.H. Teo, T. Nishino, W. Yerazunis, J. Barnwell, J. Zhang, Experimentss on wireless power transfefer with metamaterials. Appl. Phys. Lett. **98**, 254101 (2011)
16. S. Durant, Z. Liu, N. Fang, X. Zhang, Theory of optical imaging beyond the diffraction limit with a far-field superlens. Plasmon. Metal Nanostruct. Opt. Prop. IV Proc. SPIE **6323**, 63231H (2006)
17. M. Memarian, G.V. Eleftheriades, Evanescent-to-propagating wave conversion in sub-wavelength metal strip gratings IEEE Trans. Antennas Propag. **60**, 3893 (2012)
18. L. Zhaowei, S. Durant, H. Lee, Y. Pikus, N. Fang, Y. Xiong, C. Sun, X. Zhang, Far-field optical superlens. Nano Lett. **7**, 403 (2007)
19. S. Durant, Z. Liu, J.M. Steele, X. Zhang, Theory of the transmission properties of an optical far-field superlens for imaging beyond the diffraction limit. J. Opt. Soc. Am. B **23**, 2383 (2006)

20. Z. Liu, N. Fang, T.J. Yen, X. Zhang, Rapid growth of evanescent wave by a silver superlens. Appl. Phys. Lett. **83**, 5184 (2003)
21. N. Fang, H. Lee, C. Sun, X. Zhang, Sub-diffraction-limited optical imaging with a silver superlens. Science **308**, 534 (2005)
22. S.V. Pushpakaran, M. Mani, M. Pezholil, A. Chndroth, V. Kesavath, J Phys. Commun. **2**, 055005 (2018)
23. J.B. Pendry, A.J. Holden, D.J. Robbins, W.J. Stewart, Magnetism from conductors and enhanced nonlinear phenomena. IEEE Trans. Microw. Theory Tech. **47**, 2075 (1999)
24. M.J. Lockyear, A.P. Hibbins, J.R. Sambles, Microwave surface-plasmon-like modes on thin metamaterials. Phys. Rev. Lett. **102**, 073901 (2009)
25. A.P. Hibbins, B.R. Evans, J.R. Sambles, Experimental verification of designer surface plasmons. Science **308**, 670 (2005)
26. B.I. Popa, S.A. Cummer, Direct measurement of evanescent wave enhancement inside passive metamaterials. Phys. Rev. E **73**, 016617 (2006)
27. R.W. Ziolkowski, A.D. Kipple, Electrically small antennas in the presence of nested metamaterial shells. Phys. Rev. E **721**, 5 (2011)
28. U. Deepak, T.K. Roshna, C.M. Nijas, P. Mohanan, Compact CPW fed electrically small antenna for WLAN applications. IET Electron. Lett. **50**, 62 (2014)
29. H.L. Zhu, X.H. Liu, S.W. Cheung, T.I. Yuk, Frequency-reconfigurable antenna using metasurface. IEEE Trans. Antennas Propag. **62**, 80 (2014)
30. Y. Guo, X. Ma, M. Pu, X. Li, Z. Zhao, X. Luo, High-efficiency and wide-angle beam steering based on catenary optical fields in ultrathin metalens. Adv. Opt. Mater. **6**, 1800592 (2018)

Int. J. Electron. Commun. (AEÜ) 117 (2020) 153095

Contents lists available at ScienceDirect

International Journal of Electronics and Communications (AEÜ)

journal homepage: www.elsevier.com/locate/aeue

Regular paper

Broadband non-resonant split ring resonator-based artificial high dielectric substrate

PV. Anila [a,b], VP. Sarin [c], M. Manoj [a], M. Remsha [a], P. Mohanan [a,*]

[a] Centre for Research in Electromagnetics and Antenna, Dept. of Electronics, CUSAT, India
[b] M A College of Engineering, Kothamangalam, India
[c] Department of Electronics, Govt. College, Chittur, India

ARTICLE INFO

Article history:
Received 16 November 2019
Accepted 22 January 2020

Keywords:
Slot antenna
Metamaterial
Split Ring Resonator (SRR)
Permittivity

ABSTRACT

This paper presents a technique of using magnetic metamaterial as a broadband non-resonant artificial high dielectric substrate for achieving enhanced radiation performance in the microwave region. The selected metamaterial (MTM) is the basic single split-ring resonator (SRR) printed on a bare dielectric substrate of permittivity 3.8. When it is electrically excited by a plane wave, a high permittivity of 25 for the frequency range of 0.5–3.1 GHz is achieved. The application of the artificially made high dielectric substrate is validated with a 1.3 dBi gain enhancement of a broadband slot antenna with a single finite transmitter array of 5 × 4 high dielectric metamaterial substrate. The MTM-antenna composite is having an overall size of 60 × 48 × 21.6 mm^3 when printed on a substrate of dielectric constant 3.8 and height 1.6 mm. The detailed study of MTM unit cell and the effect of MTM on antenna performance is thoroughly studied in simulation and validated with free space measurements.

1. Introduction

Metamaterial creates an advancing world of design with materials along with improvements in the electromagnetic characteristics of existing systems. The concept of artificial materials explained by Veselago in 1968 and experimental verification by Pendry et al. [1] and Smith [2] opened a new horizon of metamaterial research. Smith et al. constructed a composite "medium" of negative permittivity and negative permeability in the microwave regime by arranging periodic arrays of small metallic wires and split-ring resonators [3–5] and demonstrated the anomalous property of negative refraction in this artificially made composite. The popular constituent among the metamaterial structures to offer the negative permeability is SRR which is having two concentric rings separated by a gap, both having splits at opposite sides. The equivalent circuit models, magnetic properties, spurious radiation suppression, nonlinearity, and superdirectivity of SRR's are reported widely in [6–9], etc. In [6], the authors studied the electromagnetic behavior of these elements, as well as their coupling to the host transmission line, and proposed the analytical equivalent-circuit models for the isolated and coupled SRR's in detail which enables the researchers to design various artificial materials. The potential applications of the category include antenna miniaturization, bandwidth enhancement, directivity/gain enhancement, etc.

The free space transmission and the reflection measurements of a single negative (SNG) and composite double negative (DNG) metamaterial are explained clearly in [10]. Extraction of effective permittivity and permeability of SRR's, wires and SRR-wire combination from reflection and transmission coefficients were given by Smith et al. [11]. They used the transmission and reflection coefficients calculated for a wave normally incident on a finite slab of metamaterial where the magnetic field is oriented perpendicular to the slab and the electric field being oriented axially. The effective permittivity and permeability is depending on the orientation of the electric and the magnetic fields as studied in [12]. The authors found that the incident electric field couples to the magnetic resonance of the SRR when the EM waves propagate perpendicular to the SRR plane and the incident E-field is parallel to the gap-bearing sides of the SRR. Different excitation techniques for metamaterial unit cells together with its permittivity/permeability and/or refractive index are there in [12–15]. The studies on SRR's are still going on; the researchers are exploring the different characteristics and its structural modifications.

In recent days metamaterials are widely used as the right candidate for enhancing the radiation characteristics of the antenna where the researchers are concentrating on the resonant negative

* Corresponding author.
E-mail address: drmohan@gmail.com (P. Mohanan).

https://doi.org/10.1016/j.aeue.2020.153095
1434-8411/

region of the structures and its' applications. They have used the near-zero permittivity/permeability/refractive index region for getting the directional properties of radiation patterns [16–19]. In recent studies, metamaterial superstrates are configured either as artificial magnetic conductors (AMC), frequency selective surfaces (FSS) or Electro-magnetic bandgap (EBG) structures for improving the radiation characteristics of microstrip antenna [20–22]. The various methods for enhancing the patch antenna gain are discussed theoretically in [23]. Among them the popular one is with a high dielectic cover. Shen et al. in 2000 [24] used a 25.7 × 25.7 cm^2 high dielectric superstrate of relative permittivity of 10.8 to enhance the gain of a probe-fed microstrip patch antenna by 10 dBi around 9 GHz. Various designs of artificially engineered materials for enhancing the gain and efficiency of planar antennas are reported widely in [25–35]. The paper [34] also used artificially engineered substrates designed to be anisotropic and present high dielectric constants for the waves propagating orthogonal to metallic layers. However, the designed artificial inclusions exhibited relative permittivity comparable with that of the host substrate. They made use of four layers of superstrates to achieve a front-to-back ratio greater than 10 dB with a gain enhancement around 2 dB for a frequency range of 9–12 GHz. The potential of planar artificial dielectric layers (ADL) in antenna gain enhancement is also explained in [34]. The authors in [35] used a metasurface fabricated on high dielectric material of dielectric constant 15 as a superstrate of microstrip dual-band patch antenna to improve the gain by 1–2 dB. All the reported designs only took advantage of the resonant negative/near-zero permittivity/permeability regions of metamaterials to improve the gain, directivity or bandwidth of antenna systems which suffers from the downsides of narrow bandwidth and critical design parameters. Also each and every problem and application is addressed with new designs of MTM structures. Some designs utilized extra backing reflectors. Most of the reported articles employed multiple layers of metamaterials to enhance the gain of antenna. This will increase the size and system complexity. Hence development of a single layer broadband artificial dielectric superstrate is relevant in the present scenario.

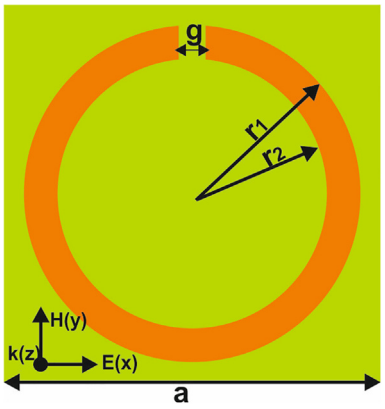

Fig. 1. Structure of a unit cell with its dimensions and field orientations: r_1 = 5 mm, r_2 = 4 mm, g = 1 mm, a = 12 mm.

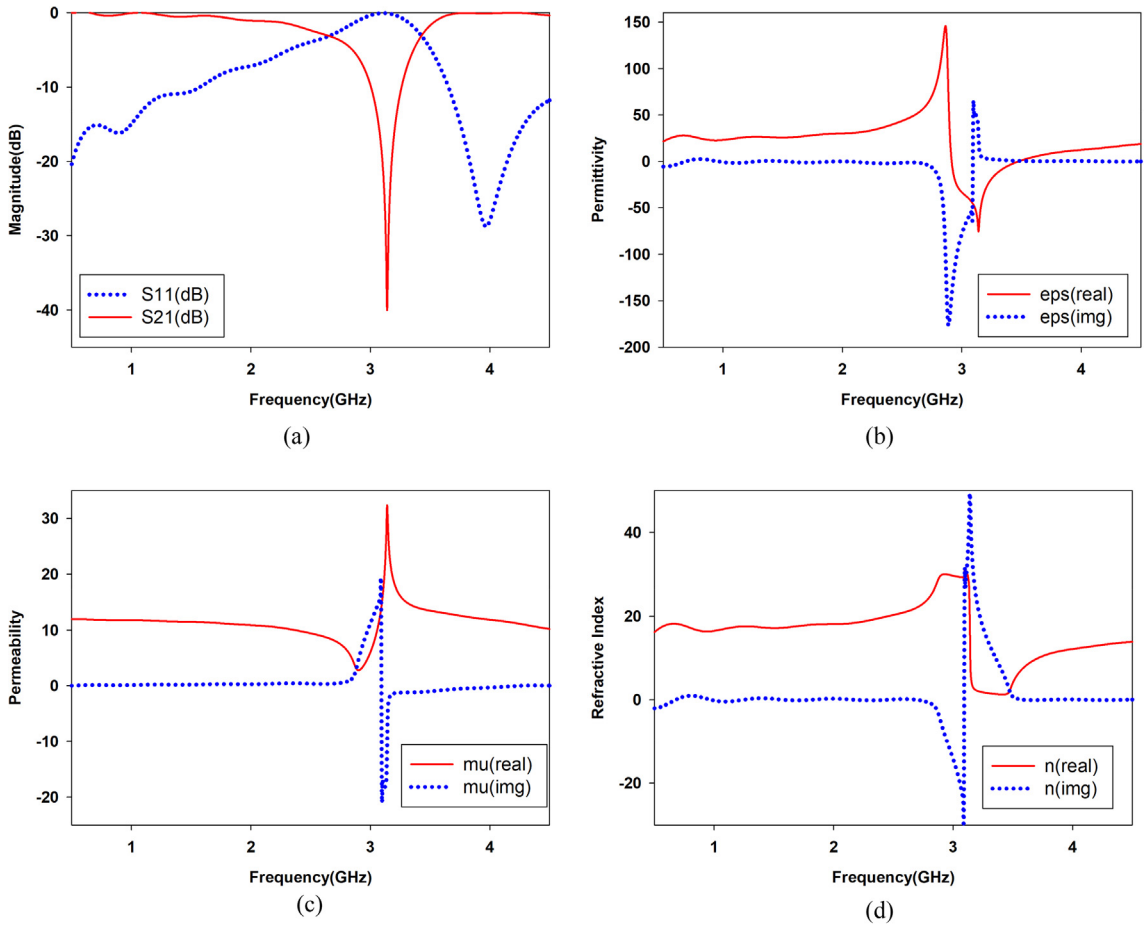

Fig. 2. (a) Reflection and transmission Coefficients. (b) Extracted Permittivity. (c) Permeability. (d) Refractive Index of Unit cell Structure.

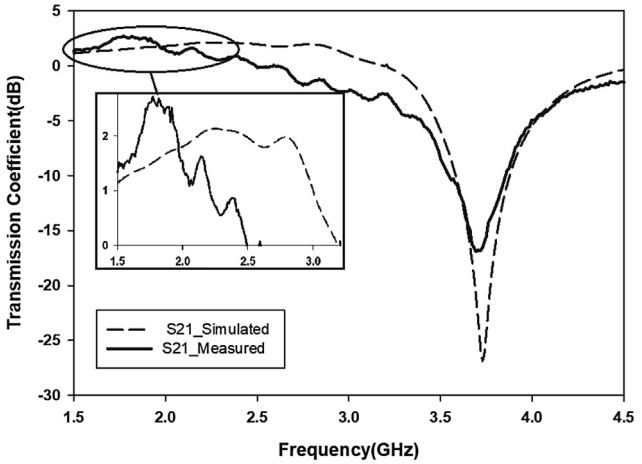

Fig. 3. Simulated and measured transmission coefficients of metamaterial full structure with the zoomed view on inset.

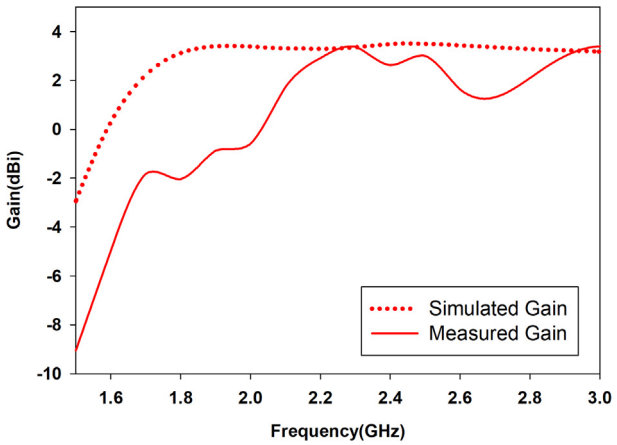

Fig. 5. Simulated and measured slot antenna gain without using superstrate.

This article presents a novel idea of using any magnetic MTM array in its non-resonant broadband region as an ADL. The authors explain the feature using an array of basic single ring SRR. The SRR array printed on a bare radiator of dielectric constant 3.8 when electrically excited by a plane wave shows a high positive value of permittivity for a broad frequency range together with the popular negative characteristics. This can replace the high cost ceramic high dielectric materials which are brittle. The example of antenna superstrate application of the same where a 5 × 4 array of metamaterial superstrate placed over a broadband slot antenna operating at 1.88 to 3 GHz to enhance the antenna gain is discussed in later sections. The designed ADL could be easily integrated with planar antenna for multiple applications thus reducing the time and fabrication cost for designing multiple MTM antenna superstrates. Arora et al. in [36] also used SRR array as antenna superstrate but with wire strips as a DNG medium and with large size to enhance the gain. The study is as follows: - characterization of the artificial dielectric substrate, its possibility as antenna superstrate, antenna design, experiments with the artificial dielectric loaded antenna utilizing the above principle.

2. Characterization of artificial dielectric substrate

The geometry of the structure is derived from those reported in [1]. The schematic view of the proposed SRR unit cell structure along with the field vectors are shown in Fig. 1. The structure is fabricated on a substrate of dielectric constant 3.8, the thickness of 1.6 mm and a loss tangent of 0.01. An SRR of outer and inner radii of 5 mm and 4 mm with a slit gap of 1 mm is used for the present study. This SRR is resonating at 3.31 GHz. The structure is devoid of any vias and metallic ground plane which makes it simple, uniplanar and easy for fabrication. The structure is characterized by the Electromagnetic simulation tool CST Microwave Studio and measurements are done using PNA E8362B vector network analyzer.

Zhou et al. in [15] explains different excitation schemes and resonant nature of a U shaped SRR for different field orientations. The most cited property of SRR is the negative permeability at a low-frequency (ω_m). This has been achieved by exciting the SRR with an external magnetic field perpendicular to the plane of SRR. One can observe an electrical resonance or negative permittivity at a higher frequency (>ω_m) by an external electric field. The SRR array exhibits a short wire like response near to ω_m with the incident electric field, parallel to the slit length of SRRs. The slab of SRR array gives almost constant high value of permittivity till ω_m. Also this type of excitation is easily achieved using planar antennas, the SRR array could be loaded as the artificial dielectric layer to improve the gain of planar antenna [23].

A uniform plane wave is incident along Z-axis where electric field and magnetic fields are along X and Y axes respectively as shown in Fig. 1. The electric field is parallel to the line joining the slit of SRR whereas the magnetic field aligns with the plane

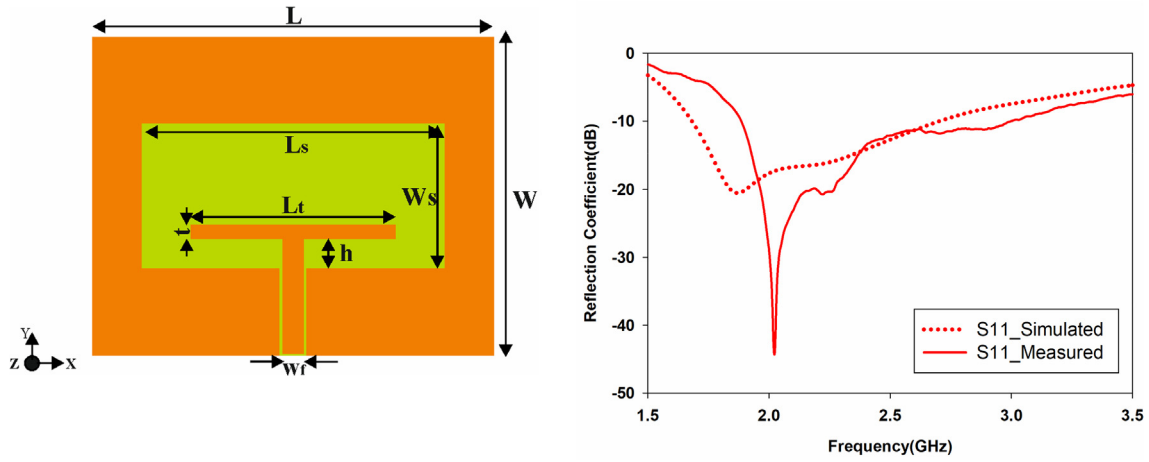

Fig. 4. (a) Wideband slot antenna geometry: L = 57 mm, W = 45 mm, Ls = 43 mm, Ws = 20.4 mm, L_t = 29 mm, t = 2 mm, W_f = 3 mm, h = 4.2 mm. (b) Simulated and measured Reflection Coefficient.

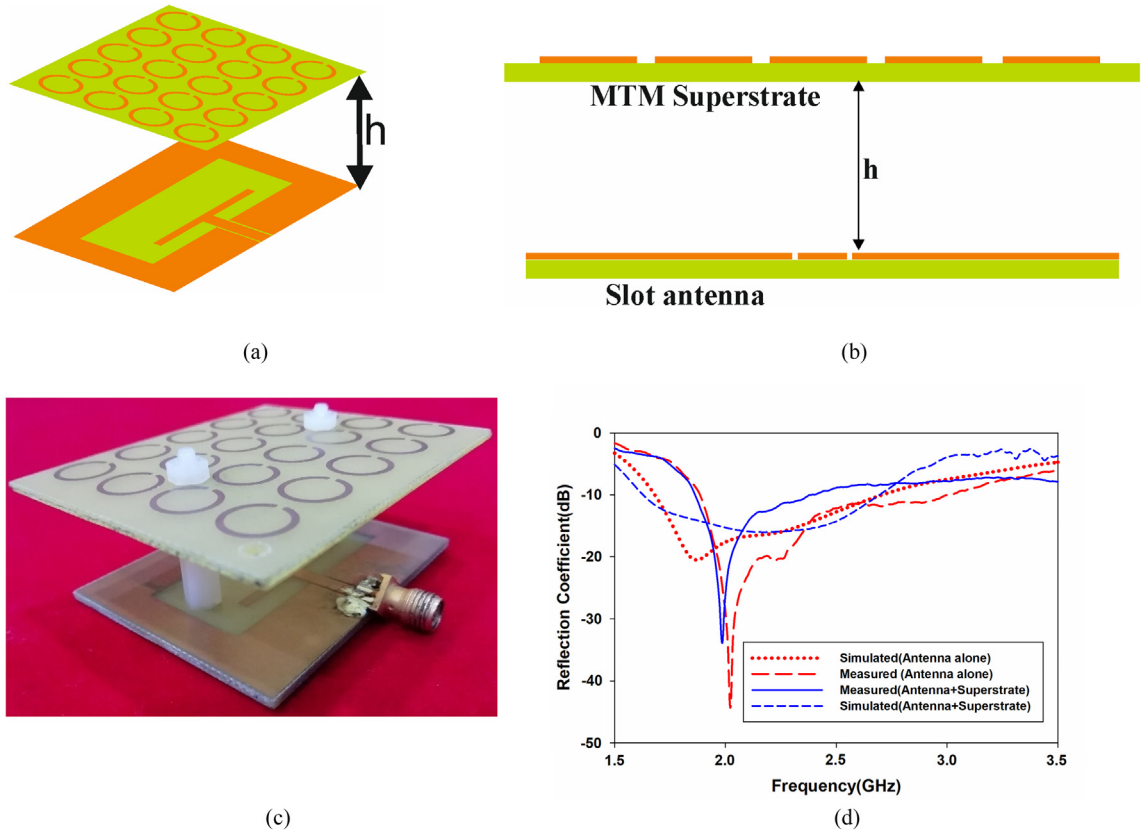

Fig. 6. (a) Geometry of slot antenna with metamaterial. (b) Side view of antenna. (c) Photograph of fabricated antenna loaded with superstrate. (d) Simulated and measured reflection coefficient of the antenna with and without metamaterial superstrate.

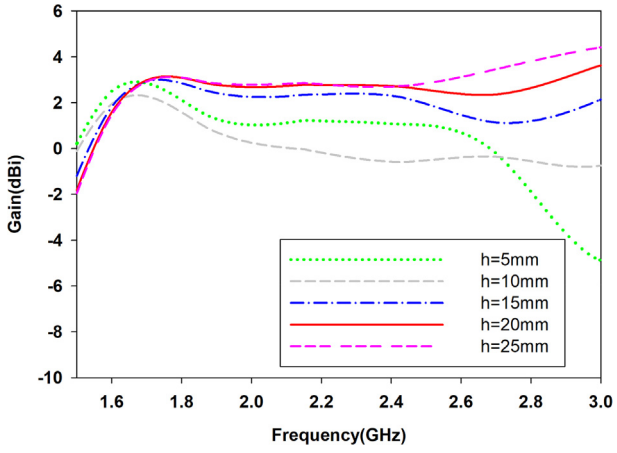

Fig. 7. Simulated antenna gain for different metamaterial superstrate loading height (h).

of SRR. A unit cell of 12 × 12 mm^2 dimensions is simulated for infinite periodic arrangement and its reflection and transmission parameters are plotted in Fig. 2(a). The transmission coefficient is high at lower frequencies and shows a dip at 3.13 GHz indicating maximum reflection. Therefore the unit cell allows maximum transmission till the resonant frequency. The permittivity and permeability of unit cell extracted [37–38] using CST Microwave Studio for a Z directed uniform plane wave with electric and magnetic fields oriented along X and Y directions are shown in Fig. 2(b) and (c). Fig. 2(d) shows the refractive index obtained from the unit cell simulations. The electrical response is excited due to the wave polarization incident on the unit cell of sub-wavelength dimension. So it will work as a reflector for this region as the reflection coefficient is maximum. The results are well-known for the SRR like structures as indicated.

Considering the frequency region below the resonant frequency of 3.13 GHz where we call it as non resonant region; the simulated permittivity is clearly showing a positive value with a maximum magnitude at 2.85 GHz with an average value of 25 and a high refractive index. The high dielectric constant and high refractive index region could be configured as an ADL enhanced superstrate for the gain improvement of conventional microstrip antennas as in [23] without changing their current geometry, size, feed or position. The ADL enhanced superstrate with a high dielectric constant is acting as a denser medium along the direction of propagation of EM waves radiated from the source radiator. Hence it improves the directivity of radiation [23]. The article proposes the application of broadband high permittivity region till the resonant frequency of metamaterial for the gain enhancement of printed antennas operating at the same frequency region. This theory is validated with the simulation and measurement results of a slot antenna loaded with a metamaterial superstrate for the gain enhancement.

A metamaterial superstrate structure with an array of 5 × 4 unit cells has been designed to align with the size of the reference slot antenna described in Section 3. The SRR array is used to verify the power-enhancing capacity of metamaterial structure; a single layer of the full structure is simulated with plane wave excitation of E field along X-axis and probes along the direction of propagation. The S-parameters retrieved from probe fields for the full structure simulation and the measured transmission characteris-

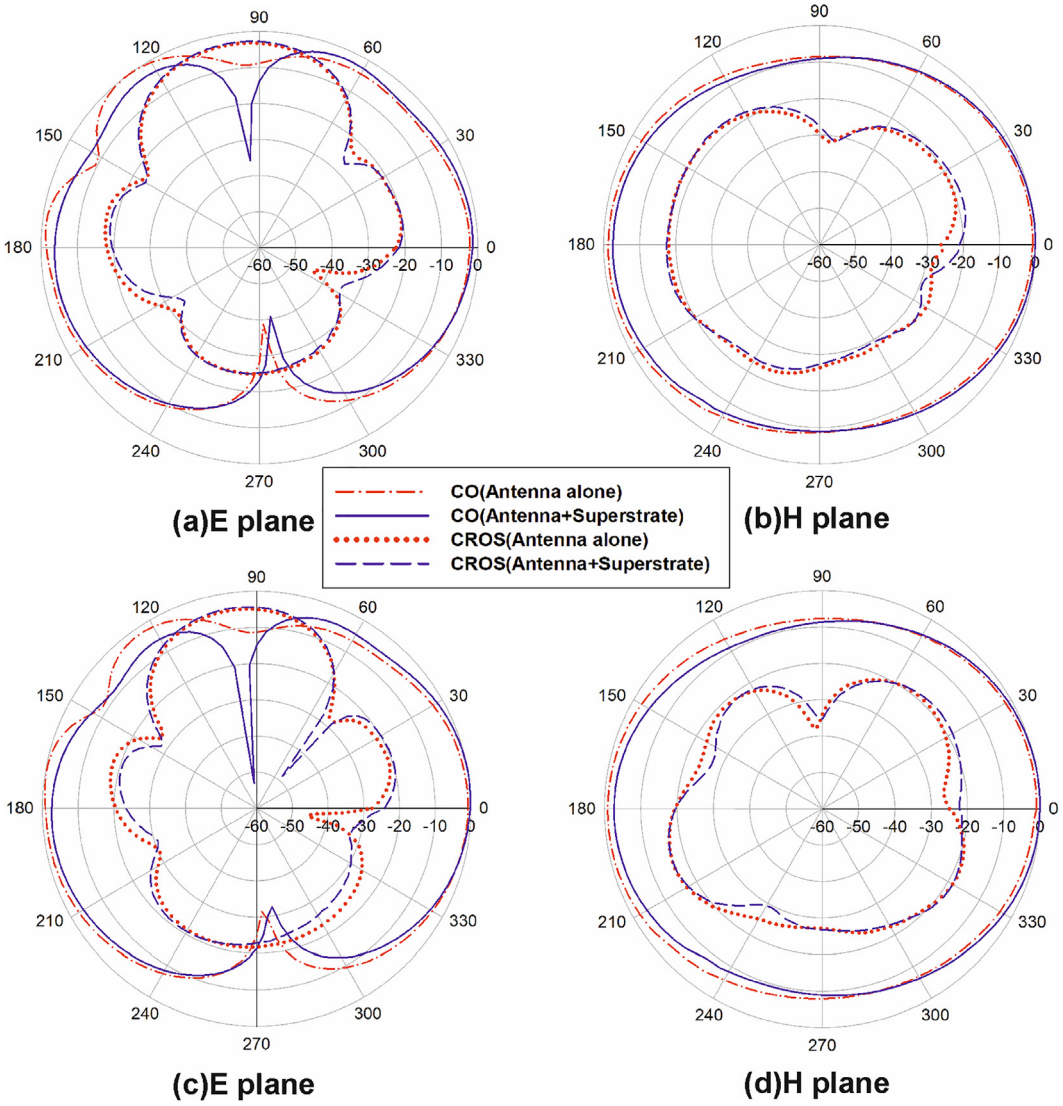

Fig. 8. Measured radiation pattern of the antenna with and without metamaterial superstrate (a), (b) for 2 GHz (c), (d) for 2.28 GHz.

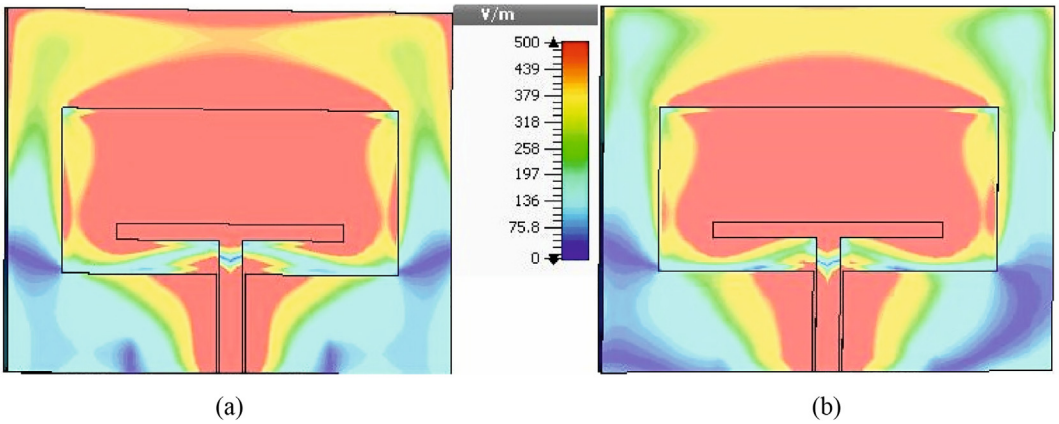

Fig. 9. E-field distributions for (a) antenna without metamaterial superstrate and (b) antenna with metamaterial superstrate.

tics for metamaterial full structure is depicted in Fig. 3 and it shows a transmission dip at 3.7 GHz with a considerable rise of approximately 2 dB in transmission coefficient for the frequency range of 1.65–1.97 GHz which is a clear indication of power enhancement capacity of the structure for the particular range and it goes down below 0 dB after 2.5 GHz. It is clear from the Fig. 2(a) and Fig. 3 that the transmission coefficient shows a dip and reflection coefficient shows a peak after 2.5 GHz for the SRR

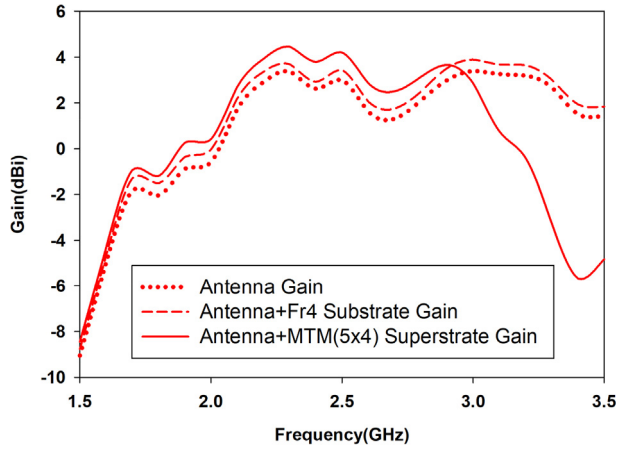

Fig. 10. Measured antenna gain with and without metamaterial superstrate.

Table 1
The performance comparisons of Reference and MTM loaded antenna.

Property	Reference Antenna	MTM Loaded Antenna
2:1 VSWR Band	1.88–3 GHz	1.86–2.41 GHz
Peak Gain (2.28 GHz)	3.5 dBi	4.8 dBi
HPBW	85.7°	75.7°
Efficiency (2.28 GHz)	95.40	94.61

array. Hence the structure can be deployed for the power enhancement from 0.5 to 2.5 GHz and the equivalent power enhancement will be proportional to the dielectric constant realized by the metamaterial structure. The measurement of the transmission coefficient of the metamaterial full structure is carried out by standard horn antenna procedures. The metamaterial sheet of SRR array is placed in between two ultra-wideband horn antennas with the corresponding fields for excitations of the unit cell as in Fig. 1. The lower frequency is restricted to 1.5 GHz due to the limitations of the measuring system.

The property of power enhancement is validated by making the metamaterial full structure as antenna superstrate to enhance the gain of the antenna described in Fig. 4(a) operating in between 1.5 GHz and 2.5 GHz. Section 3 describes the geometry and analysis of broadband slot antenna with and without the metamaterial superstrate.

3. Characterization of the reference slot antenna

The geometry of the antenna fabricated on a substrate of permittivity 3.8 and height 1.6 mm is shown in Fig. 4(a) with its geometrical parameters. It is a modified CPW fed wideband slot antenna structure [39] for the required frequency of operation. The slot antenna is selected due to its inherent wideband capacity to check the gain enhancement for a broad range of frequencies. The reflection characteristics of the slot antenna exhibit a 2:1 VSWR bandwidth of 1.12 GHz (1.88–3 GHz) as shown in Fig. 4(b) with an overall dimension of 57 × 45 × 1.6 mm^3. The difference in measured and simulated characteristics can be attributed to fabrication tolerance and slight permittivity change of the substrate. The gain chart for the antenna is shown in Fig. 5 which shows a peak gain of 3.5 dBi at 2.28 GHz. The efficiency is measured using conventional wheeler cap method and is 95% within the resonant region.

The antenna with the above radiation characteristics is loaded with the metamaterial superstrate. The metamaterial superstrate array of 5 × 4 single SRR structures with an inter elemental spacing of 2 mm is designed and fabricated. The superstrate array with an overall dimension of 60 × 48 mm^2 is placed over the antenna at a 20 mm height. The SRR is kept in such a way that the polarization of the antenna is parallel to the slit length of the SRR as explained in Section 2. The geometry, side view and photograph of the loaded antenna structure are shown in Fig. 6(a)-(c) respectively. The effect of metamaterial superstrate loading on the antenna reflection characteristics is exhibited in Fig. 6(d).

The antenna is loaded with the superstrate in the near field region which will cause a slight variation in the impedance matching of the antenna system. A parametric study has been done to optimize the loading height of the metamaterial superstrate above the antenna element (h) to improve the gain characteristics. It has been noted that as the height above the antenna (h) increases it improves the gain of the system indicated in Fig. 7 except for h = 10 mm. Analyzing the antenna characteristics at a superstrate height of 10 mm, antenna radiation is less as compared to other superstrate heights and the power absorption seems to be more. Without compromising the overall dimension and physical stability of the antenna system with moderate gain enhancement, the superstrate height (h) is taken as 20 mm. The measured far-field components of radiation pattern of the antenna with and without metamaterial for two different frequencies are plotted in Fig. 8.

The pattern clearly shows a power enhancement along the forward direction in both E-plane and H plane as proposed by the metamaterial full structure analysis explained in Fig. 3 for the frequencies. The E-field distribution on the radiating face of antenna without and with MTM superstrate is depicted in Fig. 9(a) and (b) respectively. So, it is found that the electric field is more concentrated towards center and directive on the antenna face for an antenna loaded with metamaterial superstrate. The gain enhancement for an antenna with metamaterial superstrate underlying the proposed method is measured using the gain comparison method as depicted in Fig. 10. The figure clearly emphasizes the validity of the principle with a maximum gain enhancement of 1.3 dBi giving a peak gain of 4.8 dBi around the resonance of the slot antenna on which the metamaterial is loaded without using any additional backing layers.

The antenna gain is improved for the frequency range of 1.6–2.85 GHz for the slot antenna which is resonating from 1.88 GHz to 3 GHz as depicted in Fig. 4(b) with a maximum of 95% of measured efficiency. The lower frequency of 1.6 GHz is attributed to the resonance of the antenna whereas the upper boundary of 2.85 GHz is limited by the resonating behavior and power

Table 2
The performance comparisons with earlier reported works.

Reference	Center Frequency (GHz)	No. of Superstrate layers	Spacing with antenna (mm)	Overall Size of antenna (mm^2)	Overall Size of antenna in terms of λ	Gain enhancement (dB)
25	2.55	2	41	315 × 315	2.68λ × 2.68λ	10
34	10	4	2.35/layer	120 × 120	4λ × 4λ	2
40	5.8	1	20	100 × 100	1.93λ × 1.93λ	2.3
Our Work	**2.28**	**1**	**20**	**60 × 48**	**0.46λ × 0.36λ**	**1.3**

enhancement of the metamaterial structure designed. The comparison of radiation properties of reference antenna with and without metamaterial superstrate is depicted in Table 1.

The improvement of the radiation properties of an antenna is proportional to the ADL enhanced dielectric constant [34]. Various methods employed to extract the metamaterial characteristics of the unit cell clearly define the negative resonant regions whereas they fail to indicate the magnitudes of the permittivity and permeability. All these issues are addressed in [37]. The authors also face the problem to extract the exact magnitudes of permittivity and permeability. However, we try to compare the permittivity of the designed MTM unit cell with a dielectric substrate of the same size and permittivity 4.4. From Fig. 10 it is clear that the gain enhancement of MTM superstrate is rather more as compared to the FR4 dielectric substrate used and hence its permittivity. The gain enhancement is again a function of angle of incidence from the radiator source [34]. The authors used the normal incidence for simple design and hence 1.3 dBi will be the minimum gain improvement obtained from the ADL enhanced superstrate. The practicality of the above said principle and design lie in the fact that the antenna designers can improve the gain of presently deployed integrated antenna structures without changing their geometry, position or feed. Again, it reduces the design complexity in metamaterial superstrates as it provides a general design to use in multiple application bands in broad frequency range. Also the gain enhancement is achieved without any additional backing ground layers as in [40].

Most of the metamaterials for improving the gain of antennas are acting either as AMC's and/or Artificial Magnetic Materials (AMM's) as explained in the introduction part. Researchers had done a few works in the area where metamaterials used as an artificial high permittivity substrate consolidated in Table 2 where λ is the free space wavelength corresponding to center frequency. It clearly emphasis the important part of the proposed method. The proposed method gives the maximum gain enhancement for minimum number of superstrate layers and minimum size for lowest frequency of operation. Also noted that the antenna with metamaterial superstrate improves the gain along with improving the power radiated characteristics of the antenna; the important concept in antenna design.

4. Conclusion

The authors presented a novel method to artificially synthesize high dielectric constant substrates used to improve the radiation properties of microstrip antenna in this paper. The technique includes applying electrically excited metamaterial in the non-resonant broadband region to enhance the gain of the existing printed planar antenna. The method gives the feasibility to get a single design for multiple applications for broad frequency range hence reducing the design complexity. The ADL enhanced dielectric superstrate material could be manufactured cheaply and placed on top of antenna without a fine alignment between the two. The novelty of the technique is that the method could be put in to practice for the radiation characteristics improvement of currently deployed antennas without changing their geometry, feed or position. Also, the high permittivity superstrate is fabricated with a low-cost commonly available substrate which makes it cost-effective. The antenna and superstrate structures are uniplanar which makes it simple in fabrication. The paper demonstrates the effectiveness of the method by enhancing the gain by 1.3 dBi of a wideband slot antenna with a metamaterial superstrate structure without using a backing ground. The power enhancement is proportional to the dielectric constant achieved by the metamaterial superstrate. Also larger aperture size of the array can increase the gain even more.

Declaration of Competing Interest

The authors declare that they have no known competing financial interests or personal relationships that could have appeared to influence the work reported in this paper.

Acknowledgment

For research support, Anila P.V. acknowledges KTU-CERD, Govt. of Kerala under Research Seed Money scheme and the authors gratefully acknowledge the facilities and support given by Advanced Centre for Atmospheric Radar Research, CUSAT and DST PURSE scheme provided to Cochin University of Science and Technology by DST, Govt. of India.

References

[1] Pendry JB, Holden AJ, Robbins DJ, Stewart WJ. Magnetism from conductors and enhanced nonlinear phenomena. IEEE Trans Microw Theory Tech 1999;47:2075–84.
[2] Smith DR, Padilla WJ, Vier DC, Nemat-Nasser SC, Schultz S. Composite medium with simultaneously negative permeability and permittivity. Phys Rev Lett 2000;84:4184–7.
[3] Smith DR, Kroll N. Negative refractive index in left-handed materials. Phys Rev Lett 2000;85:2933–6.
[4] Shelby RA, Smith DR, Nemat-Nasser SC, Schultz S. Microwave transmission through a two-dimensional. Isotropic, left-handed metamaterial. Appl Phys Lett 2001;78:489–91.
[5] Shelby A, Smith DR, Schultz S. Experimental verification of a negative index of refraction. Science 2001;292:77–9.
[6] Baena Juan Domingo, Bonache Jordi, Martín Ferran, Sillero Ricardo Marqués, Lopeteg Txema, Laso Miguel AG, et al. Equivalent-circuit models for split-ring resonators and complementary split-ring resonators coupled to planar transmission lines. IEEE Trans Microwave Theory Tech 2005;53:1451–61.
[7] Chen HS, Ran LX, Huangfu JT, Zhang XM, Chen KS. Magnetic properties of S-shaped split-ring resonators. Prog Electromagn Res 2005;51:231–47.
[8] Lee Jae-Gon, Lee Jeong-Hae. Suppression of spurious radiations of patch antennas using split-ring resonators (SRRs). Microwave Opt Technol Lett 2006;48:283–7.
[9] Wang Bingnan, Zhou Jiangfeng, Koschny Thomas, Soukoulis Costas M. Nonlinear properties of split-ring resonators. Opt Express 2008;16:16058–63.
[10] Ozba Ekmel, Aydin Koray, Cubukcu Ertugrul, Bayindir Mehmet. Transmission and reflection properties of composite double negative metamaterials in free space. IEEE Trans Antennas Propag 2003;51(10):2592–5.
[11] Smith DR, Schultz S, Markos P, Soukoulis CM. Determination of effective permittivity and permeability of metamaterials from reflection and transmission coefficients. Phys Rev B 2002:65.
[12] Katsarakis N, Koschny T, Kafesaki M, Economou EN, Soukoulis CM. Electric coupling to the magnetic resonance of split-ring resonators. Appl Phys Lett 2004;84(15).
[13] Aydin Koray, Bulu Irfan, Guven Kaan, Kafesaki Maria, Soukoulis Costas M, Ozbay Ekmel. Investigation of magnetic resonances for different split-ring resonator parameters and designs. New J Phys 2005;7:168.
[14] Gay-Balmaz Philippe, Martina Olivier JF. Electromagnetic resonances in individual and coupled split-ring resonators. J Appl Phys 2002;92(5).
[15] Zhou Jiangfeng, Koschny Thomas, Soukoulis Costas M. Magnetic and electric excitations in split ring resonators. Opt. Express 2007;15(26).
[16] Dakhli Saber, Rmili Hatem, Mahdjoubi Kouroch, Floc'h Jean-Marie, Choubani Fethi. A family of directive metamaterial-inspired antennas. Prog Electromagn Res C 2014;49:105–13.
[17] Zhou H, Pei Z, Qu S, Zhang S, Wang J, Li Q, et al. A planar zero-index metamaterial for directive emission. J Electromagn Waves Appl 2009;23 (7):953–62.
[18] Arora Chirag, Pattnaik Shyam S, Baral Rudra N. SRR superstrate for gain and bandwidth enhancement of microstrip patch antenna array. Prog Electromagn Res B 2017;76:73–85.
[19] Attia Hussein, Yousefi Leila, Bait-Suwailam Mohammed M, Boybay Muhammed S, Ramahi Omar M. Enhanced-gain microstrip antenna using engineered magnetic superstrates. IEEE Antennas Wirel Propag Lett 2009;8.
[20] Das Satyadeep, Sahu Sudhakar. Design of high gain, broadband resonant cavity antenna with meta-material inspired superstrate. Int J Electron Commun 2019;100:39–46.
[21] Vaid Swati, Mittal Ashok. High gain planar resonant cavity antennas based on metamaterial and frequency selective surfaces. Int J Electron Commun (AEÜ) 2015;69:1387–92.

[22] Jam Shahrokh, Simruni Mojtaba. Performance enhancement of a compact wideband patch antenna array using EBG structures. Int J Electron Commun (AEÜ) 2018;89:42–55.
[23] Jackson David R, Alexopoulos Nicolaos G. Gain enhancement methods for printed circuit antennas. IEEE Trans Antennas Propag 1985;33(9).
[24] Shen Xiao-Hai, Delmotte Peter, Vandenbosch Guy AE. Enhancing the gain of microstrip antennas at different frequencies with one substrate-superstrate structure. Microw Opt Technol Lett 2000:27.
[25] Weng Zi-bin, Wang Nai-biao, Jiao Yong-chang, Zhang Fu-shun. A directive patch antenna with metamaterial structure. Microw Opt Technol Lett 2007;49.
[26] Fresidis A, Goussetis G, Wang S, Vardaxoglou JC. Artificial magnetic conductor surfaces and their application to low-profile high-gain planar antennas. IEEE Trans Antennas Propag 2005;53(1):209–15.
[27] Mosallaei H, Sarabandi K. Magneto-dielectrics in electromagnetics: concept and applications. IEEE Trans Antennas Propag 2004;52(6):1558–67.
[28] Buerkle A, Sarabandi K. A wide-band, circularly polarized, magneto dielectric resonator antenna. IEEE Trans Antennas Propag 2005;53(11):3436–42.
[29] Lovat G, Burghignoli P, Capolino F, Jackson DR. Combinations of low/high permittivity and/or permeability substrates for highly directive planar metamaterial antennas. IET Microwaves Antennas Propag 2007.
[30] Sáenz Elena, Gonzalo Ramón, Ederra Iñigo, Vardaxoglou John C, de Maagt Peter. Resonant meta-surface superstrate for single and multifrequency dipole antenna arrays. IEEE Trans Antennas Propag 2008;56:951.
[31] Kim Dongho, Choi Jaeick. Analysis of antenna gain enhancement with a new planar metamaterial superstrate: an effective medium and a Fabry-Pérot resonance approach. Springer; 2010.
[32] Attia H, Siddiqui O, Ramahi OM. Artificial magneto-superstrates for gain and efficiency improvement of microstrip antenna arrays. PIERS Online. 2010;6:555.
[33] Attia Hussein, Siddiqui Omar, Yousefi Leila, Ramahi Omar M. Metamaterial for gain enhancement of printed antennas: theory, measurements, and optimization. Procee. of Saudi international electronics, communications, and photonics conference (SIECPC), 2011.
[34] Syedand Waqas H, Neto Andrea. Front-to-back ratio enhancement of planar printed antennas by means of artificial dielectric layers. IEEE Trans Antennas Propag 2013;61:5408–10.
[35] Islam Mohammad Tariqul, Ullah Mohammad Habib, Singh Mandeep Jit, Faruque Mohammad Rashed Iqbal. A new metasurface superstrate structure for antenna performance enhancement. Materials 2013;6:3226–40.
[36] Arora Chirag, Pattnaik Shyam S, Baral RN. Performance enhancement of patch antenna array for 5.8 GHz Wi-MAX applications using metamaterial inspired technique. Int J Electron Commun (AEÜ) 2017;79:124–31.
[37] Chen Xudong et al. Robust method to retrieve the constitutive effective parameters of metamaterials. Phys Rev E 2004;70.
[38] Smith David et al. Electromagnetic parameter retrieval from inhomogeneous metamaterials. Phys Rev E 2005;71.
[39] Chagharvand Sahar, Hamid MR, Kamarudin MR, Khalily Mohsen. Wideband slot antenna for 4G applications. In: Procee. of IEEE Asia-Pacific conference on applied electromagnetics (APACE). p. 279–81.
[40] Kim Jae Hee, Ahn Chi Hyung, Bang Jin-Kyu. Antenna gain enhancement using a holey superstrate. IEEE Trans Antennas Propag 2016:64.

Applied Physics A (2020) 126:90
https://doi.org/10.1007/s00339-019-3270-9

Applied Physics A
Materials Science & Processing

Toroidal dipole-induced coherent forward scattering from a miniaturized cloaking structure

V. P. Sarin[1] · P. V. Vinesh[1] · M. Manoj[2] · C. K. Aanandan[2] · P. Mohanan[2] · K. Vasudevan[2]

Received: 2 November 2019 / Accepted: 26 December 2019

Abstract
The physical existence of microwave toroidal dipole in a dogbone metallic inclusion-based miniaturized cloaking structure is verified in this paper. The excitation of toroidal dipole moments on the studied composite is verified using multipole scattering formalism. The presence of the toroidal Fano resonance significantly enhances resonant forward scattering from the structure for normal incidence. Multipolar contribution from the electric, magnetic and toroidal moments significantly enhances the scattering cross-section of the composite as compared to a bare cylindrical metallic object. Applicability of the proposed scheme is tested inside an anechoic chamber using reflection measurements on the fabricated structure and is subsequently validated in computer simulations in the microwave frequency regime.

Keywords Dogbone metamaterial · Forward scattering · Toroidal dipole

1 Introduction

Electromagnetic scattering from objects having sub-wavelength dimensions compared to the incident radiation is a topic of great interest for the electromagnetic community [1]. The scattering studies of magneto-dielectric materials are of great importance in this era of metamaterials. The incident electromagnetic waves induce electric and magnetic polarizability on these particles whose values can be controlled by varying the structural and constitutive parameters. Kerker pointed out some unusual scattering properties of magneto-dielectric objects with selected permittivity and permeability values [2]. If the induced crossed electric and magnetic polarizabilities are equal and if they are oscillating in phase, then this combination can be treated as a Huygens's source. This combination gives high forward scattering with backward scattering suppressed [3] and could be used for achieving super directive radiation from electrically small sources and antennas [4–6]. If the electric and magnetic moments are oscillating out of phase, then the composite gives zero scattering cross-section and could be termed as "invisible bodies" [7]. If we can control the magnitude and phase of induced electric and magnetic dipole moments, then unprecedented control of electromagnetic wave propagation could be achieved. But due to the lack of natural magnetic materials at microwave and optical wavelengths, this problem remained unsolved until the introduction of Pendry's invention of artificial magnetism using split-ring resonators [8]. The invention of metamaterials is treated as a paradigm shift in the field of electromagnetics, because the magnitude and phase of induced electric and magnetic dipole moments could be tailored independently thereby controlling both phase and magnitude of reflection and transmission of electromagnetic waves [9, 10].

Recently, there is immense interest in the scattering studies of a special type of excitation, known as toroidal dipoles in composite metamaterial structures. As pointed out earlier, the classical electromagnetic theory accounts for only the electric and magnetic dipoles in multipole scattering formalism [11]. Toroidal dipoles are exempted from classical multipole scattering expansion and their excitation is significantly weak in ordinary metamaterial composites. Their excitation was first reported in nuclear systems [12]. The scattering patterns of a toroidal dipole and an electric dipole are similar [13]. Toroidal excitations are used in electromagnetically induced resonant

✉ V. P. Sarin
sarincrema@gmail.com

[1] Department of Electronics, Government College Chittur, Palakkad, Kerala 678104, India

[2] Centre for Research in Electromagnetics and Antennas, Cochin University of Science and Technology, Cochin, Kerala 682022, India

Published online: 13 January 2020

transparency schemes [14]. A variety of studies are focused on this topic in the microwave frequency regime [15–17]. As a substitute for metallic implants, all-dielectric metamaterials could be successfully used for the generation of toroidal dipoles [18]. The advantage of dielectric composites is that they are devoid of losses associated with conduction currents. The simultaneous excitation of parallel electric and toroidal moments, popularly known as an anapole, could be used to reduce scattering cross-section of an object [19, 20]. An anapole resonance is characterized by a strong electromagnetic energy concentration in the near field and can be used for energy localization [21, 22]. Recently, water-based dielectric toroidal dipoles have been effectively used for achieving electromagnetic invisibility [23].

The authors recently proposed a cylindrical cloaking enclosure for scattering reduction from a metallic cylinder using dogbone inclusions [24]. Dogbone metamaterials are an alternative to the conventional split-ring resonator and cut-wire pairs for achieving negative refractive index behavior [25]. Dogbone metamaterial absorbers have been effectively used for enhancing the radiation performance of dipole antenna [26]. In this paper, the physical existence of toroidal dipole resonance is verified using a miniaturized dogbone cloaking structure. Miniaturization is achieved using only one dogbone element along the radial direction and by reducing the radius of the cylindrical metal target. The advantage of the proposed design is that the presence of toroidal Fano resonance greatly enhances forward scattering at resonance in comparison with a bare metallic cylinder. Full-wave electromagnetic simulation studies are carried out using the CST Microwave Studio platform and the experiments are performed inside an anechoic chamber using PNA E8362B network analyzer.

2 The geometrical description

The unit cell of the proposed miniaturized structure is depicted in Fig. 1. A hollow metallic cylinder with a reduced radius (r) of only 0.5 mm is used as the cylindrical target under consideration in comparison with our previous design [24]. The main difference is that only one dogbone cell is used around the target along radial direction such that there are a total of eight dogbone elements in the unit cell around the cylinder as shown in Fig. 1a. The distributed dogbone-shaped particles with dimensions indicated in Fig. 1b are printed on an epoxy substrate of relative dielectric constant 4.4 and height 1.6 mm. The final structure is formed by repeating five such cells along Z-direction, such that there are 40 dogbone cells in the composite. The height of the cylinder is 160 mm. Standard photolithography is used for the fabrication of dogbone metallization. The thickness of the engraved copper metallic layer is 35 µm. The geometric parameters of the dogbone metallization are $L_1 = 18$ mm, $L_2 = 12$ mm, $W_1 = 4$ mm and $W_2 = 2$ mm.

3 Results and discussion

Reflection coefficient of the proposed structure is measured for normal incidence using monostatic RCS measurement setup inside an anechoic chamber. Numerical simulations have been performed on the target using the full-wave solver

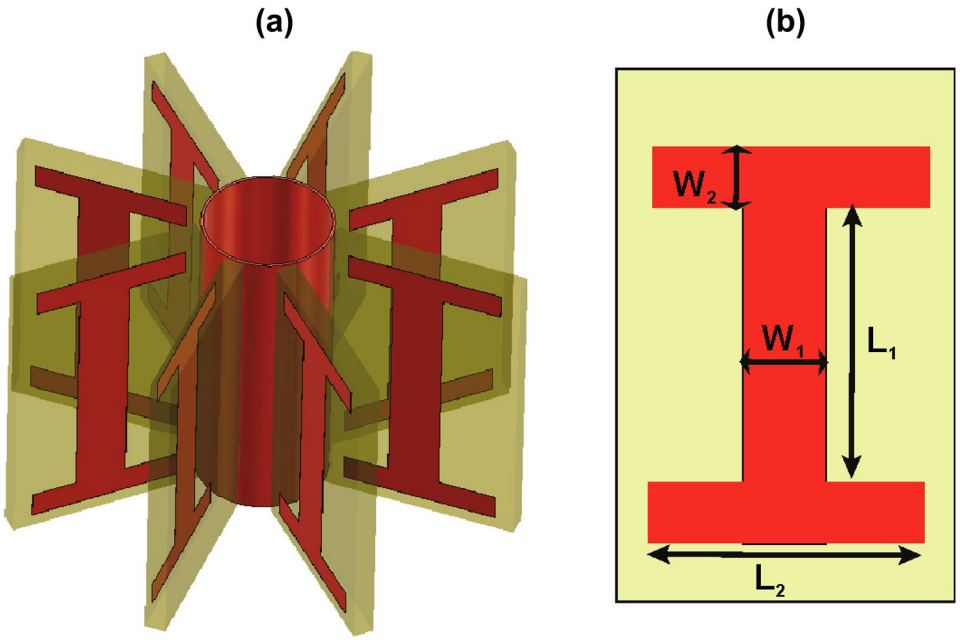

Fig. 1 Geometry of the cloaking scheme: **a** construction of the unit cell and **b** geometrical specifications of dogbone metallization

CST Microwave Studio. The full structure is simulated in the frequency domain with a normally incident plane wave with polarization parallel to the metallic cylinder. The measured and simulated reflection coefficient of the structure normalized with respect to the bare metallic cylinder is depicted in Fig. 2a. The resonance is identified at 2.16 GHz and the small mismatches are accounted due to fabrication tolerances. The geometry of the fabricated prototype used for measurement is illustrated in Fig. 2b.

CST simulations have been performed to validate the results obtained from reflection measurements. In the computational domain, the cylinder is oriented along the *Y*-axis and the wave allowed propagating from the left to the right along *Z*-axis. The results of computations performed on the cloaked target at 2.16 GHz are depicted in Fig. 3. Figure 3a depicts the magnitude of E_y component of the electric field along the *YZ* plane of the computational domain. It is obvious that the composite smoothly transfers the impinging electromagnetic field into the exit face of the structure. For further clarifying the transmission characteristics, the Poynting vector distribution at resonance is taken into consideration and is depicted in Fig. 3b. It is seen that the structure routes the incident electromagnetic waves around the target and a smooth flow of power is observed on the exit face.

To have a clear idea about the scattering characteristics of the structure for a normally incident plane wave, the scattering studies are performed in simulations and the results are summarized in Fig. 4. Scattering from the target is characterized by measuring the radar cross-section (RCS) and scattering cross-sections (SCS) in CST Microwave Studio. Radar cross-section or back scattering cross-section is defined as:

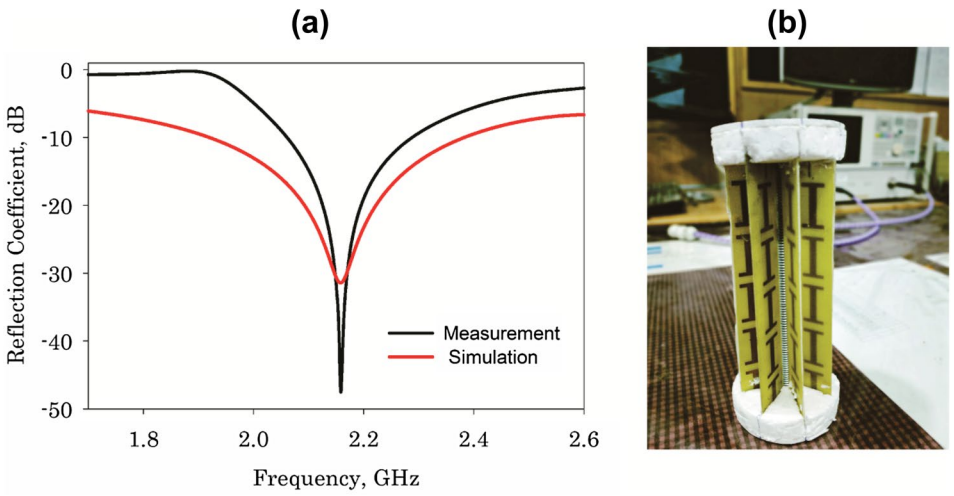

Fig. 2 **a** Reflection coefficient from the composite and **b** geometry of the fabricated sample

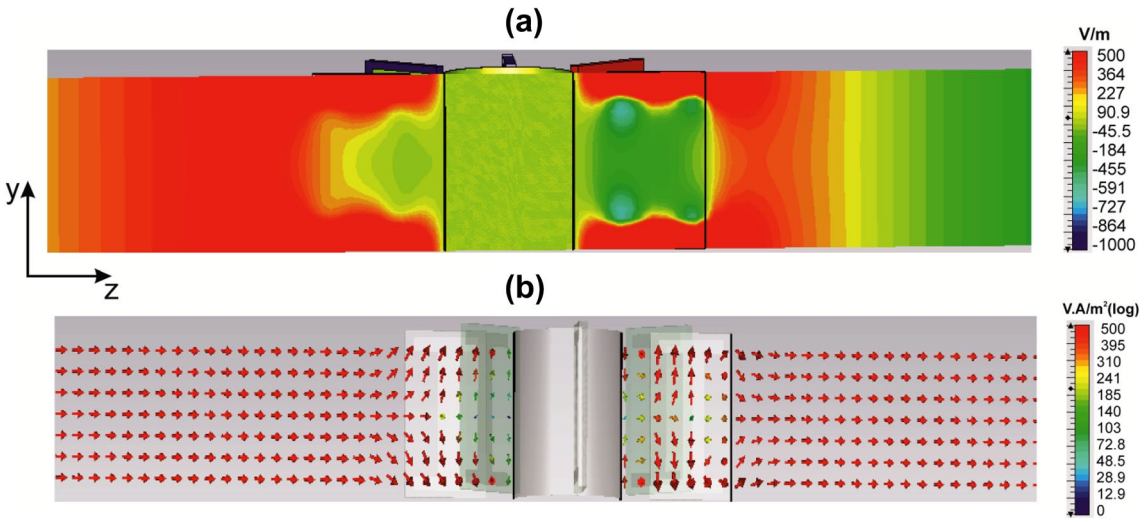

Fig. 3 Results of numerical simulation for the cloaked target at 2.16 GHz **a** electric field distribution from the *YZ* plane and **b** pointing vector distribution from the *YZ* plane

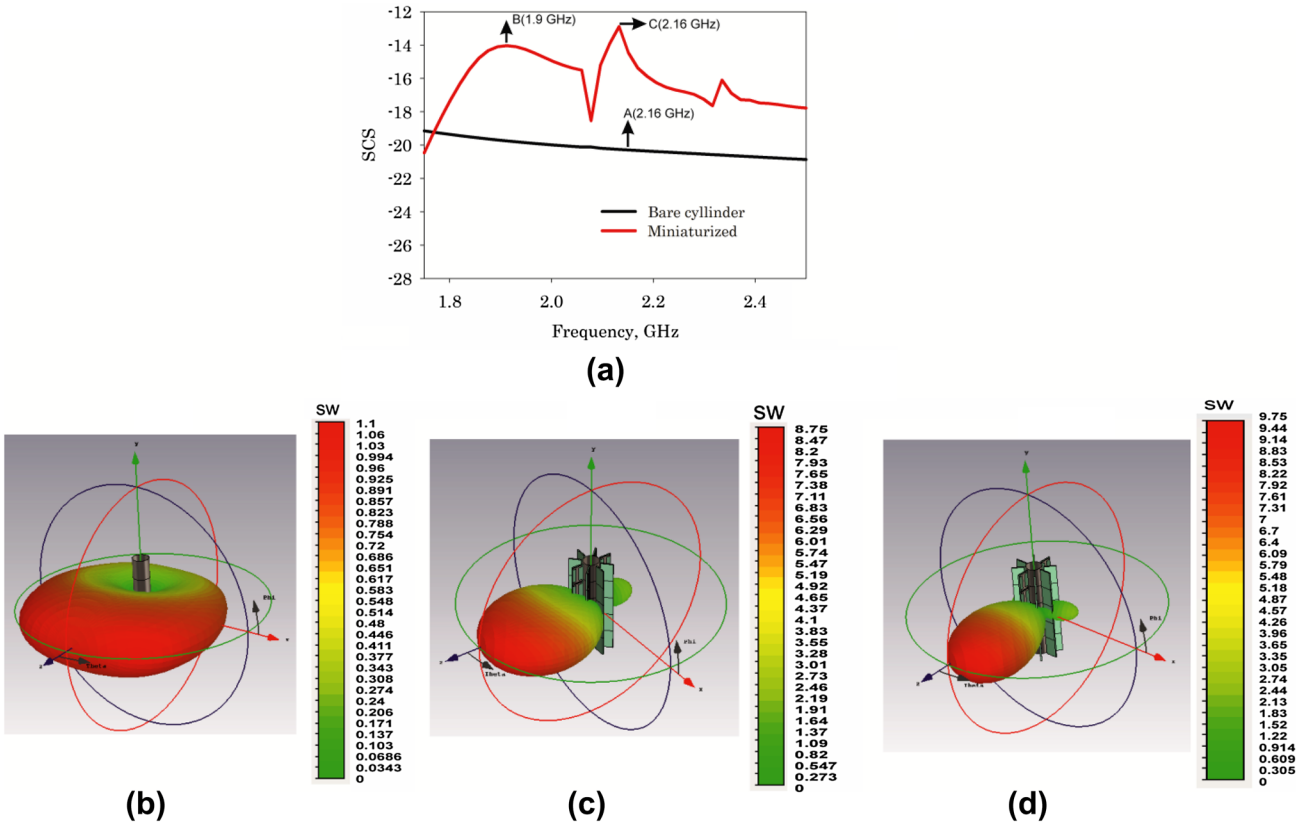

Fig. 4 Scattering characteristics of the structures: **a** SCS of the metallic cylinder with and without dogbone inclusions, **b** RCS of the bare metallic cylinder at 2.16 GHz (point *A*), **c** RCS of the bare metallic cylinder with dogbone cover at 1.9 GHz (point *B*), and **d** RCS of the bare metallic cylinder with dogbone cover at 2.16 GHz (point *C*)

$$\sigma = \lim_{R\to\infty} 4\pi R^2 \frac{|E_{\text{sca}}|^2}{|E_{\text{inc}}|^2}, \tag{1}$$

where R is the distance from the target to the observation point, E_{inc} is the incident electric field measured at the position of the target, E_{sca} is the scattered electric field measured at the observation point. If this quantity is zero, it means that the scattered power from the target at the far-field location is zero. The scattering cross-section is another important parameter usually used with cloaking problems. It is defined as:

$$\sigma_{\text{total}} = \frac{1}{4\pi} \int \sigma \mathrm{d}\Omega, \tag{2}$$

where the integration of σ is performed over the whole solid angle around the target. The SCS of the bare metallic cylinder and that of the miniaturized structure are shown in Fig. 4a. The SCS of the proposed structure shows substantial improvement throughout the entire frequency band in comparison with the bare metallic cylinder. Maximum enhancement in SCS has been observed at the resonant frequency of 2.16 GHz where the reflection from the structure is minimum. This scattering behavior is entirely different from our earlier work in which the resonance is characterized by a low SCS. Figure 4b–d represents the RCS of the frequency points represented in by points *A*, *B*, and *C* in Fig. 4a. Point *A* represents the sampling point of the bare metallic cylinder and at this frequency, the cylinder scatters power equally along the azimuth plane of the computational domain as represented in Fig. 4b. Here, only the electric dipole moment is present and the acute scattering is offered by this P_y component. The inclusion of dogbone elements with the cylinder is equivalent to the creation of magnetic dipole moments on the structure. Figure 4c, d represents the RCS of the cylinder with dogbone inclusions at 1.9 GHz and 2.15 GHz, respectively. Both of these frequency points show a coherent forward scattering pattern in comparison with the bare metallic cylinder. The lower peak at 1.9 GHz is characterized by an RCS of 9.42 dBsw with a 3 dB beam width of 102.7° along the azimuth plane. The higher peak at 2.16 GHz is showing an RCS value of 9.89 dBsw and shows highly coherent forward scattering with a 3 dB beamwidth of 72.9° along the azimuth plane.

To clarify the reason behind this peculiar scattering behavior, multipole scattering theory has been utilized to

retrieve the resonant mechanism of the miniaturized structure [14]. Scattered power from the induced multipoles could be calculated by integrating the spatially distributed current distribution over the unit cell. The multipole amplitudes can be calculated as:

$$P = \frac{1}{i\omega}\int J\mathrm{d}^3 r, \tag{3}$$

$$M = \frac{1}{2c}\int (\vec{r}XJ)\mathrm{d}^3 r, \tag{4}$$

$$T = \frac{1}{10c}\int [(\vec{r}.J) - 2r^2 J]\mathrm{d}^3 r, \tag{5}$$

where P is the electric dipole moment, M is the magnetic dipole moment, T is the toroidal moment, c is the velocity of light in vacuum, $\underset{r}{\rightarrow}$ is the displacement vector from the origin, ω is the angular frequency and J is the surface current density retrieved from simulations. The total power radiated from different multipole moments can be formulated as:

$$I = \frac{2\omega^4}{3c^3}|P|^2 + \frac{2\omega^4}{3c^3}|M|^2 + \frac{2\omega^6}{3c^5}|T|^2 + \cdots \tag{6}$$

Corresponding radiated powers from the electric (P_y), magnetic (M_x) and toroidal (T_y) dipole moments are illustrated in Fig. 5. It is observed that at resonance, the electric dipole moment is showing a strong dip. Throughout the entire frequency of operation, the magnitude of power scattered by the magnetic dipole moment is of the order greater than 1000 than that of the electric dipole moment. The interesting fact is that the structure also shows a significant contribution from the toroidal dipole moment T_y. As the frequency is increased, the power scattered from this T_y component also shows significant improvement. So the peculiar enhanced forward scattering is caused due to the presence of toroidal moments on the structure.

To gain a deep understanding of the resonant field distribution on the structure, the magnetic field distribution and the resonant current distribution excited on the structure for normal incidence at resonance are depicted in Fig. 6a, b, respectively. It is clear from the current distribution that three neighboring dogbone elements located at the entrance phase of the wave are excited in phase. The surface currents excited on the metallic cylinder are out of phase with that in these dogbone inclusions along Y-axis. The resulting circulating currents on the dogbone and the metal target create magnetic moment M_x on the composite. The resulting magnetic vortex formed between these adjacent inclusions as shown in Fig. 6a creates the toroidal polarizability T_y on the composite. These circulating surface currents are equivalent

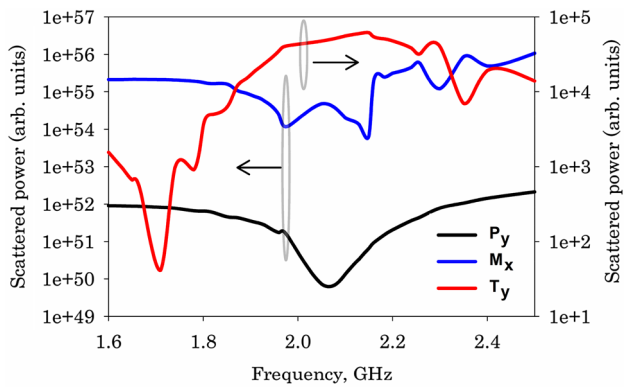

Fig. 5 Radiated power from different multipoles

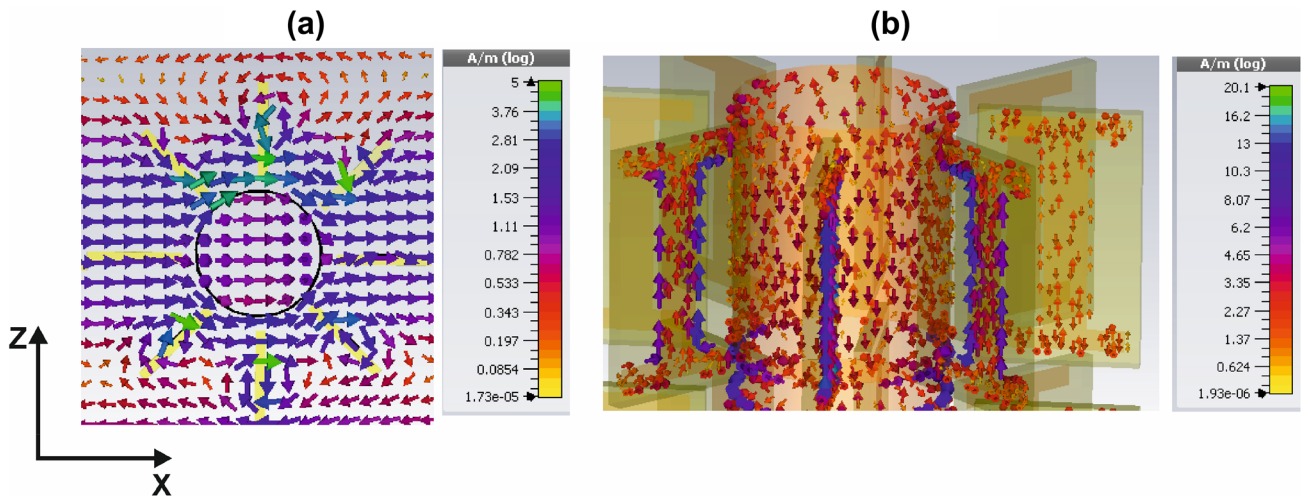

Fig. 6 Simulated field distributions at 2.16 GHz **a** magnetic field distribution and **b** surface current distribution

to that observed in conventional toroidal geometries. It is noted from Fig. 6b that the magnetic polarization is induced on each dogbone cell by the anti-parallel current distributions existing on the metallic target and the dogbone metallization along *Y*-direction. The out-of-phase currents circulating in between the dogbone cells and the metallic cylinder reduce scattering from the electric polarization and hence a dip is found in the power scattered from the electric polarization P_y. From these observations, it can be concluded that the resonant mechanism behind this particular scattering behavior is the excitation of toroidal Fano resonant modes on the composite. Fano resonance is the superposition of a spectrally broad scattering resonance and an asymmetrical narrow dark resonant mode [27]. The spectrally broad non-resonant scattering is offered by the metallic cylinder itself and the magnetic resonant mode is accounted by the circulating currents on the composite. The backscattered power is reduced here due to the destructive interference between these modes and forward scattering is aided due to constructive interference. The proposed structure will be useful for the generation of highly directional radiation from electric dipole antennas in the microwave frequency regime. In the conventional microwave and millimeter-wave antennas, high directivity is achieved by combining electric and magnetic dipole resonances [28]. The creation of toroidal polarizability in such systems could strongly increase the directivity of the system.

The frequency dependence of RCS has also been analyzed through simulation studies and these results are summarized in Fig. 7. Figure 7a–c shows the 3D RCS pattern at 2 GHz, 2.16 GHz, and 2.4 GHz, respectively. It is obvious that the resonance at 2.16 GHz is showing a highly coherent forward scattering with backward scattering suppressed in comparison with the two other frequency points. The lower resonance at 2 GHz is characterized by severe backscattering in comparison with the forward scattered power. At 2.4 GHz, the structure shows a broad-beam scattered pattern along the forward direction. The high coherence at resonance is caused

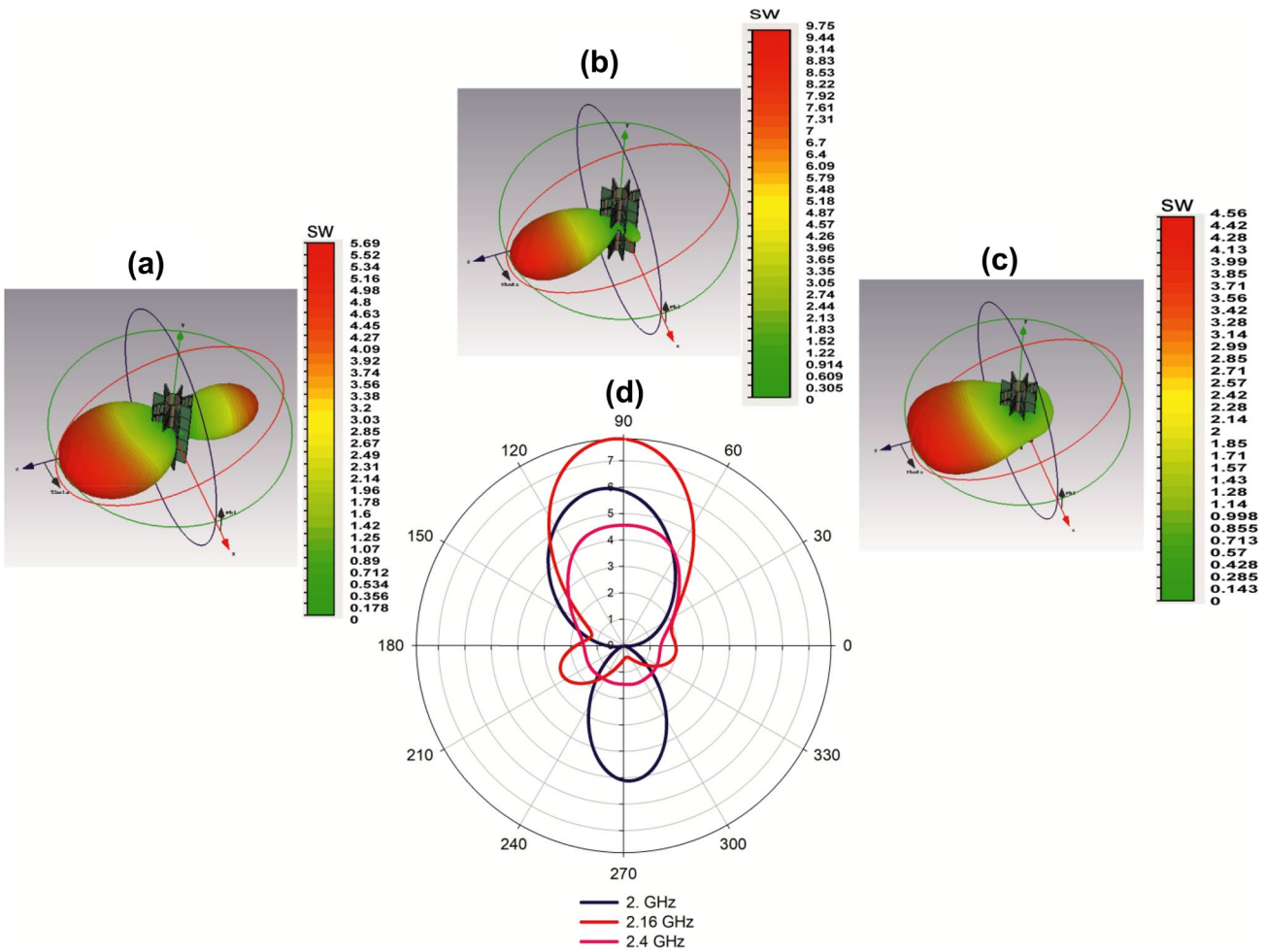

Fig. 7 Scattering characteristics of the structure for different frequencies: **a** 3D pattern at 2 GHz, **b** 3D pattern at 2.16 GHz, **c** 3D pattern at 2.4 GHz, and **d** 2D polar plot representing scattering patterns at these frequencies along the azimuth plane

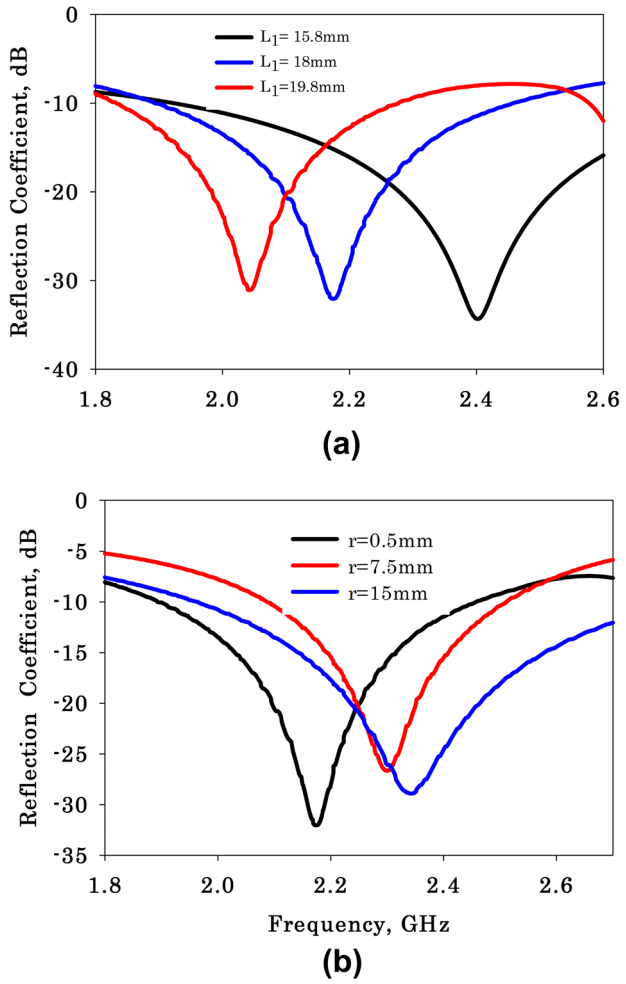

Fig. 8 Parametric variations on the unit cell: **a** effect of variation in dogbone vertical length (L_1) and **b** effect of variation in target diameter (r)

due to the resonant excitation of the toroidal dipole moment in the composite. Figure 7d illustrates the 2D polar scattered power pattern from the composite at these three frequency points. At 2 GHz, the structure shows significant backscattering and the 3 dB beamwidth is found to be 96.8°. The significant excitation of toroidal dipole moment significantly reduces the backward scattering at 2.16 GHz and it shows a 3 dB beamwidth of 72.9° yielding enhanced coherence along the forward direction. Hence, this frequency point could be used for achieving super directive radiation from finite-sized antennas. As frequency increases, the 3 dB beamwidth starts decreasing and at 2.4 GHz, the beam width is found to be 115.7°.

Parametric analysis has been performed on the structure for studying the effect of various parameters on reflection characteristics. The effect of variation on dogbone vertical parameter L_1 and the radius of the target 'r' are illustrated in Fig. 8. The parameter L_1 is varied, while other parameters are kept constant. The radius of the target is fixed here as $r = 0.5$ mm. It is obvious from Fig. 8a that an increase in the dogbone height significantly shifts the resonant frequency towards the lower side. This due to the increase in the inductance caused by the increased metal strip which alters the self-electric resonance of the dogbone metallization and the combined magnetic resonance of the composite. Figure 8b illustrates the effect of the target radius on reflection characteristics. It is noted that the increase in the radius of the target shifts the resonant frequency towards the higher side.

4 Conclusions

The physical existence of microwave toroidal dipole moment in a miniaturized cloaking structure in the microwave regime is presented in this paper. Multipolar decomposition reveals that at resonance there is a significant contribution from the toroidal dipole moment resulting in an enhanced coherent forward scattering. The presence of the toroidal dipole moment significantly enhances the scattering cross-section of the structure in comparison with a bare metallic cylinder. The proposed scheme surely paves way for the creation of super directivity and Bessel-like beams in the microwave regime.

Acknowledgements The authors acknowledge the research funding received from the Science and Engineering Research Board (SERB), Department of Science and Technology for the major research project ECR/2017/002204.

References

1. C.F. Bohren, D.R. Huffman, *Absorption and Scattering of Light by Small Particles* (Wiley, Hoboken, 1983)
2. M. Kerker, D.S. Wang, L. Giles, Electromagnetic scattering by magnetic spheres. J. Opt. Soc. Am. **73**, 765–767 (1983)
3. T.A. Milligan, *Modern Antenna Design* (Wiley, Hoboken, 2005)
4. P. Alitalo, A.O. Karilainen, T. Niemi, C.R. Simovski, S.A. Tretyakov, Design and realisation of an electrically small Huygens source for circular polarization. IET Microw. Antennas Propag. **5**, 783–789 (2011)
5. R.W. Ziolkowski, Low profile, broadside radiating, electrically small Huygens source antennas. IEEE Access **3**, 2644–2651 (2015)
6. R.W. Ziolkowski, Using Huygens multipole arrays to realize unidirectional needle-like radiation. Phys. Rev. X **7**, 031017 (2017)
7. A.E. Miroshnichenko, B. Luk'yanchuk, S.A. Maier, Y.S. Kivshar, Optically induced interaction of magnetic moments in hybrid metamaterials. ACS Nano **6**, 837–842 (2012)
8. J.B. Pendry, A.J. Holden, D.J. Robbins, W.J. Stewart, Magnetism from conductors and enhanced nonlinear phenomena. IEEE Trans. Microw. Theory Tech. **47**(11), 2075–2084 (1999)
9. B.O. Zhu, J. Zhao, Y. Feng, Active impedance metasurface with full 3600 reflection phase tuning. Nat. Sci. Rep. **49**, 1–6 (2013)

10. B.O. Zhu, K. Chen, N. Jia, L. Sun, J. Zhao, T. Jiang, Y. Feng, Dynamic control of electromagnetic wave propagation with the equivalent principle inspired tunable metasurface. Nat. Sci. Rep. **4**, 1–7 (2014)
11. J.D. Jackson, *Classical Electrodynamics*, 3rd edn. (Wiley, Hoboken, 1999)
12. I.B. Zel'dovich, The relation between decay asymmetry and dipole moment of elementary particles. Phys. JETP **6**, 1184 (1958)
13. G.N. Afanasiev, Y.P. Stepanovsky, The electromagnetic field of elementary time-dependent toroidal sources. J. Phys. A Math. Gen. **28**, 4565 (1995)
14. L.-Y. Guo, M.-H. Li, X.-J. Huang, H.-L. Yang, Electric toroidal metamaterial for resonant transparency and circular cross-polarization conversion. Appl. Phys. Lett. **105**, 033507 (2014)
15. T. Kaelberer, V.A. Fedotov, N. Papasimakis, D.P. Tsai, N.I. Zheludev, Toroidal dipolar response in a metamaterial. Science **330**, 1510–1512 (2010)
16. Manoj Gupta, Vassili Savinov, Ningning Xu, Longqing Cong, Govind Dayal, Shuang Wang,Weili Zhang, Nikolay I. Zheludev, Ranjan Singh, Sharp Toroidal Resonances in Planar Terahertz Metasurfaces., Adv. Mater. 201601611, 1–6 (2016).
17. M. Gupta, R. Singh, Toroidal versus fano resonances in high Q planar THz metamaterials. Adv. Opt. Mat. **201600553**, 1–7 (2016)
18. A.C. Tasolamprou, O. Tsilipakos, M. Kafesaki, C.M. Soukoulis, E.N. Economou, Toroidal eigenmodes in all-dielectric metamolecules. Phys. Rev. B **94**, 205433 (2016)
19. A.E. Miroshnichenko, A.B. Evlyukhin, Y.F. Yu, R.M. Bakker, A. Chipouline, A.I. Kuznetsov, B. Luk'yanchuk, B.N. Chichkov, Y.S. Kivshar, Nonradiating anapole modes in dielectric nanoparticles. Nat. Commun. **6**, 8069 (2015)
20. N.A. Nemkov, I.V. Stenishchev, A.A. Basharin, Nontrivial nonradiating all-dielectric anapole. Nat. Sci. Rep. **7**, 1064 (2017)
21. A.A. Basharin, V. Chuguevsky, N. Volsky, M. Kafesaki, E.N. Economou, Extremely high Q-factor metamaterials due to anapole excitation. Phys. Rev. B **95**, 035104 (2017)
22. P.C. Wu, C.Y. Liao, V. Savinov, T.L. Chung, W.T. Chen, Y.-W. Huang, P.R. Wu, Y.-H. Chen, A.-Q. Liu, N.I. Zheludev, D.P. Tsai, Optical anapole metamaterial. ACS Nano **12**, 1920–1927 (2018)
23. I.V. Stenishchev, A.A. Basharin, Toroidal response in all-dielectric metamaterials based on water. Nat. Sci. Rep. **7**, 9468 (2017)
24. V.P. Sarin, M.P. Jayakrishnan, P.V. Vinesh, C.K. Aanandan, P. Mohanan, K. Vasudevan, An experimental realization of cylindrical cloaking using dogbone metamaterials. Can. J. Phys. **95**, 927–932 (2017)
25. G. Donzelli, A. Vallecchi, F. Capolino, A. Schuchinsky, Metamaterial made of paired planar conductors: particle resonances, phenomena and properties. Metamaterials **3**, 10–27 (2009)
26. S.V. Pushpakaran, J.M. Purushothama, M. Mani, A. Chandroth, M. Pezholil, V. Kesavath, A metamaterial absorber based high gain directional dipole antenna. Int. J. Microw. Wirel. Technol. **10**, 430–436 (2018)
27. M.V. Rybin, P.V. Kapitanova, D.S. Filonov, A.P. Slobozhanyuk, P.A. Belov, Y.S. Kivshar, M.F. Limonov, Fano resonances in antennas: general control over radiation patterns. Phys. Rev. B **88**, 205106 (2013)
28. S.V. Pushpakaran, N.M. SeidMuhammed, R.K. Raj, A. Pradeep, P. Mohanan, K. Vasudevan, A Compact stacked dipole antenna with directional radiation coverage for wireless applications. IEEE Antenna Wirel. Propag. Lett. **12**, 841–844 (2013)